FLUID MIXING EFFICIENCY ENHANCEMENT IN MICROCHANNELS HAVING SPIRAL ELLIPTIC AND CURVED STRUCTURES WITH VARIOUS BAFFLE GEOMETRIES

by

RANA ALTAY

Submitted to the Graduate School of Engineering and Natural Sciences in partial fulfillment of the requirements for the degree of Master of Science

SABANCI UNIVERSITY

DECEMBER 2020

FLUID MIXING EFFICIENCY ENHANCEMENT IN MICROCHANNELS HAVING SPIRAL ELLIPTIC AND CURVED STRUCTURES WITH VARIOUS BAFFLE GEOMETRIES

APPROVED BY:

DATE OF APPROVAL: December 25, 2020

ABSTRACT

FLUID MIXING EFFICIENCY ENHANCEMENT IN MICROCHANNELS HAVING SPIRAL ELLIPTIC AND CURVED STRUCTURES WITH VARIOUS BAFFLE GEOMETRIES

Rana Altay

Mechatronics Engineering, M.Sc. THESIS, DECEMBER 2020

Thesis Supervisor: Prof. Dr. Ali KOŞAR

Keywords: Passive Mixing, Elliptic Spiral Microchannels, Curved Microchannels, Chaotic Advection, Dean Vortices

Passive micromixers have attracted much attention during recent years due to the low-cost and simple fabrication procedures with less power input in their implementation to high-throughput microfluidics platforms. Increasing the efficiency of micromixers could be possible with an optimum geometry of inertial microfluidic channels, which utilize Dean vortices and Dean flows for the enhancement of mixing. Recently, micromixers with curved microchannels have been introduced to the literature. Yet, the enormous potential of elliptic spiral and baffled embedded curved serpentine microchannels has not been adequately revealed.

This study aims to assess the mixing performance of polydimethylsiloxane micromixers having five-loop spiral microchannels with elliptic configurations and serpentine microchannels with a curvature angle of 280°. The elliptic spiral micromixers have different initial aspect ratios with a varying radius of curvature along the channel

whereas the serpentine micromixers with a fixed radius of curvature consist of six different baffle configurations embedded into the side walls to investigate the effect of the number and geometry of baffles on mixing efficiency. The performances of these micromixers were evaluated by comparing the mixing indices obtained from inverted fluorescence microscopy over Reynolds numbers ranging from 10 to 100 and 1 to 50 for elliptic spiral and serpentine micromixers, respectively. The development of transverse Dean flows and Dean vortices within the micromixers with elliptic spiral microchannels could provide mixing indices up to 96% at a low Reynolds number (*Re*=40) while the maximum outlet mixing indices of serpentine micromixers with quasi-rectangular baffles was 98% at a Reynolds number of 20.

ÖZET

SPİRAL ELİPTİK VE FARKLI ENGEL GEOMETRİLERİNE SAHİP KAVİSLİ MİKRO KANALLARDA AKIŞKAN KARIŞTIRMA VERİMLİLİĞİNİN ARTIRIMI

Rana Altay

Mekatronik Mühendisliği, Yüksek Lisans TEZİ, ARALIK 2020

Tez Danışmanı: Prof. Dr. ALİ KOŞAR

Anahtar Kelimeler: Pasif Karıştırma, Spiral Eliptik Mikro kanallar, Kavisli Mikro kanallar, Kaotik Adveksiyon, Dean Vortisleri

Düşük maliyetli ve kolay üretim tekniklerine sahip pasif mikro karıştırıcılar harici kaynağa ihtiyaç duymadan yüksek verimli mikro akışkan platformlara entegre edilebilmektedir. Bu nedenle yakın dönemde büyük ilgi görmüştür. Dean girdaplarının ve Dean akışların optimum şekilde kullanılabildiği atalet mikro akışkan geometrisi bulunarak karışımın verimliliğini iyileştirmek mümkündür. Bu amaçla literatürde mevcut olan kavisli mikro kanallar kullanılmıştır. Fakat, eliptik spiral ve farklı engel geometrilerine sahip kavisli mikro kanalların muazzam karıştırma potansiyeli yeterince açığa çıkarılmamıştır.

Bu çalışma, beş döngülü spiral eliptik ve 280 ° eğrilik açısına sahip kavisli mikro kanallarda karıştırma performansını değerlendirmeyi amaçlamaktadır. Eliptik spiral mikro karıştırıcılar, kanal boyunca değişen eğrilik yarıçapı ve farklı başlangıç en boy oranlarına sahipken, kavisli mikro karıştırıcılar sabit eğrilik yarıçapına ve engel sayısı ile geometrisinin karıştırma verimliliğine etkisini incelemek amacıyla kanal duvarlarına

gömülmüş altı farklı engel konfigürasyonuna sahiptir. Mikro karıştırıcıların performansları çevrik floresan mikroskobu kullanılarak elde edilen ve karşılaştırılan karıştırma indeksleri ile sırasıyla eliptik spiral ve kavisli karıştırıcılar için 10 ila 100 ve 1 ila 50 arasında değişen Reynolds sayılarında elde edilmiştir. Eliptik spiral mikro kanallarda enine Dean akışlarının ve Dean girdaplarının düşük Reynolds sayılarında (Re=40) gelişmesi ile %96'ya varan karıştırma performansı sağlanırken, yarı dikdörtgen engel geometrisine sahip mikro kanalların en yüksek çıkış karıştırma performansı 20 değerindeki Reynolds sayısında %98 olarak hesaplanmıştır.

ACKNOWLEDGEMENTS

I am thankful to the people who have made me who I am today. I remember the time I have been chosen as an undergraduate student at Sabanci University. Years past but memories and experiences stay there to evolve your soul. I would like to express my sincere appreciation to Professor Ali Koşar who believed me and allow me to pursue my Master of Science Degree in Micro-Nano Scale Heat Transfer and Microfluidics Research Laboratory with his great supervision. I have learned a lot from his knowledge and the opportunities that he provided me to be recognized in the world of academia.

I also would like to thank Assoc. Prof. Özlem Kutlu and Asst. Prof. Hüseyin Üvet for being my dissertation committee. Their valuable time and feedbacks are important to improve my study.

I would like to express my gratitude to Mükerrem İlker Sevgen who guided me and support me. I will always treasure our memories in the laboratory which became my sweet home to come every day with joy for his presence. I always learned from his experiences in life and his technical knowledge in every subject. I would also like to thank Zeki Semih Pehlivan for his endless support. He enlightens me even in everyday matters and improves my knowledge of science.

Finally, my beautiful, full of love and powerful family, who always stand by me and support me with their love. I am appreciated to have my mother Saniye Altay who is my role model and the strongest woman I have ever met in my life and my sweetheart little sister Gizem Defne Altay whose presence always makes me cheerful. I could not continue my journey without them. Pogba, my little dog, who cannot talk but express his love with all his actions, who wait for me until late at night and meet me at the door with his extreme energy, thank you for choosing me.

I would like to acknowledge the financial support provided by The Scientific and Technological Research Council of Turkey (TUBITAK) Support Program for Scientific and Technological Research Grant, 119N401 and the Sabanci University Internal Project Grant, Grant No. I.A.CF-18-01877. The utilization of the equipment and devices supported by Sabanci University Nanotechnology Research and Applications Center (SUNUM) is appreciated.

To My Father

Mehmet ALTAY

Gökler aydınlık olsun…

"Every act of creation is first an act of destruction"

Pablo Ruiz Picasso

TABLE OF CONTENTS

LIST OF FIGURES

LIST OF TABLES

LIST OF SYMBOLS

Re	Reynolds number (-)
U	Average flow velocity (m/s)
D_h	Hydraulic diameter (m)
D	Diffusivity (m^2/s)
Pe	Péclet number (-)
De	Dean number (-)
R	Radius of curvature (m)
M	Mixing index
I	Pixel intensity (-)
v.l.	Vertical Length

Greek symbols

ρ	Density (kg/$m^{3)}$
μ	Dynamic viscosity (kg/ms)
δ	Curvature ratio (-)

CHAPTER 1.

INTRODUCTION

1.1. Motivation and Literature Review

The scope of microfluidics and nanofluidics has been extending during recent years to many fields including chemistry and bioengineering. Integrated microfluidics devices enable low consumption of samples and chemicals within small confinements as well as reduced processing time and enhanced quality of the analysis. Mixing plays a crucial role in integrated microfluidics systems involving the mixing of certain compounds for many applications such as bio-analytical processes (Kim et al., 2009), biological screening (Park et al., 2005), protein folding (Bilsel et al., 2005), polymerization (Iwasaki & Yoshida, 2005; Nagaki et al., 2004), extraction (Mae et al., 2004), crystallization (Ståhl et al., 2001) and organic synthesis (Hessel et al., 2005; Jeong et al., 2010). Micromixers have been utilized to achieve mixing by increasing the contact area between fluid streams. However, in microchannels, where laminar flow conditions are mostly present, the fluid follows a rather smooth path without any disruption or swirls. Thus, the focus in many related studies is on increasing the mixing performance by manipulating fluid flow to induce chaotic advection in microchannels. According to the use of external energy sources, micromixers are categorized into active and passive micromixers.

Active micromixers operate by external energy sources such as pressure (Z. Li & Kim, 2017; Zhang et al., 2019), acoustic (Lim et al., 2019; Orbay et al., 2017), magnetic (Jeon et al., 2017), electrical (Usefian et al., 2019), and/ or thermal sources (Meng et al.,

2018) to obtain efficient mixing. Although the mixing performance of active mixers is relatively better than passive mixers for a wide range of Reynolds numbers (Bayareh et al., 2020), passive micromixers have a low-cost and require less power. The advantages such as simple fabrication procedure, less device footprint, and independence of any external source led to the extensive utilization of passive micromixers in lab-on-a-chip applications. The mixing performance of passive micromixers is mainly dependent on geometry. It is possible to induce chaotic advection and increase molecular diffusion by modifying the microchannel design.

The sub-classification of passive micromixers can be listed depending on the number of dimensions: three-dimensional (3D) and two-dimensional (2D) (Cai et al., 2017). 2D passive micromixers have an advantage over 3D passive micromixers thanks to their simpler structure, which allows an easy and fast fabrication process flow. 2D passive micromixers have different microchannel types including lamination-based channel, unbalanced collisions channel, obstacle-based channel, convergent-divergent channel, curved channel, and spiral channel (Bayareh et al., 2020; Cai et al., 2017). Lamination based micromixers consist of parallel or multi lamination structures, where mixing occurs in a straight channel. Because of the absence of Dean vortices and secondary flows, the length of straight channels needs to be longer than the mixers having a curved geometry to achieve a higher mixing performance at low Reynolds numbers (Bayareh et al., 2020; Cai et al., 2017; Gambhire et al., 2011). By modifying the orientation and/or adding different structures into the channel, the mixing efficiency can be increased (Gobby et al., 2001; Hong et al., 2004; Wong et al., 2004). The unbalanced collisions mixers were introduced to the literature by Ansari et. al. (Ansari et al., 2010), where the combination of unbalanced splits and cross collisions of the fluid and Dean vortices effects provide mixing. The design of unbalanced collision mixers mostly depends on the asymmetric geometry of the channel, which provides an asymmetric split and recombination of fluid streams (J. Li et al., 2013). Besides, the combination of unbalanced collision and convergent-divergent channel design, which causes expansion vortices by a sudden increase of the cross-section area, is employed for the enhancement in mixing. Tran-Minh et. al. (Tran-Minh et al., 2014) performed a mixing study on planar micromixers with elliptic micropillars to decrease the mixing length of human blood in the laminar flow regime using the concept of splitting and recombination. Similarly, to induce chaotic advection in microchannels, Le The et. al. (The et al., 2015) performed a mixing analysis for trapezoidal-zigzag micromixers, where multiple mixing mechanisms such as splitting, recombination, and twisting of the fluid stream and vortices were utilized for efficient mixing.

Curved micromixers have been widely used by taking the advantage of Dean vortices and transversal Dean flows in microchannels (Alam & Kim, 2012; Baheri Islami et al., 2017; Shamloo et al., 2017). For example, Akgönül et. al. (Akgönül et al., 2017) conducted a study to reveal the effect of asymmetry along a curvilinear microchannel with a 280° curvature angle at Reynolds numbers ranging from 1 to 60. Alijani et al. (Alijani et al., 2019) carried out a study in micromixers with curved serpentine microchannels to investigate the effect of curve angle for different curve angles (180°, 230°, and 280°) and Reynolds numbers from 30 to 227. The results of the largest curve angle were superior to the two other cases since this configuration provided a higher mixing efficiency at low flow rates. Recently, Mashaei et al. (Mashaei et al., 2020) numerically investigated the mixing efficiency in curved micromixers by modifying the configuration with four successive quadrant units located in a non-planar arrangement.

The mixing performance can also be improved by embedding obstacles in the center of the channels (Bhagat et al., 2007; Shi, Huang, et al., 2019; Shi, Wang, et al., 2019) or the walls of the channel (Bhagat & Papautsky, 2008; Raza & Kim, 2019; Sato et al., 2005; Wong et al., 2003). As an example, Alam and Kim (Alam & Kim, 2012) embedded rectangular grooves in the wall of a curved microchannel to observe the effect of width and depth of these obstacles. According to their results, the microchannel having rectangular baffles performed better compared to the smooth microchannel at Reynolds numbers greater than 10. Besides, they performed a numerical investigation of the effect of cylindrical obstacles, which were inserted into the channel, on the mixing performance (Alam & Kim, 2012). Bhagat et al. (Bhagat et al., 2007) conducted an experimental and numerical study over a wide range of flow rates on passive micromixers with obstructions. Wang et al. (Wang et al., 2002) obtained the optimum design parameters such as the layout and number of obstacles in Y-channels to improve the mixing performance. Similarly, Rahman Nezhad and Mirbozorgi (Rahman Nezhad & Mirbozorgi, 2018) numerically studied the effect of three different shaped baffles embedded in the walls of chaotic micromixers. The performance of the micromixers with baffles was superior.

The spiral structure of micromixers offers chaotic advection in microchannels due to the curved geometry, which utilizes transverse Dean flow and Dean vortices for the enhancement in a mixing (Al-Halhouli et al., 2015; Duryodhan et al., 2017; Mehrdel et al., 2018; Nivedita et al., 2017; Schönfeld & Hardt, 2004; Sudarsan & Ugaz, 2006). Schönfeld and Hardt introduced a mixer design based on spiral shape structure and investigated the effect of helical flow on micromixing (Schönfeld & Hardt, 2004). Later, Sudarsan and Ugaz (Sudarsan & Ugaz, 2006) performed a study in planar spiral microchannels, where five-spiral designs with different channel lengths were used to examine the mixing performance at Reynolds numbers between 0.02 to 18.6. They also reported that the mixing performance could be further enhanced by introducing the expansion vortices to the flow with a change in the cross-sectional area of the channel. Recently, a numerical and experimental study was performed by Duryodhan et. al. (Duryodhan et al., 2017). They evaluated the mixing performances of spiral micromixers with different channel aspect ratios over a wide range of Reynolds numbers ranging from 1 to 468. In another study, Nivedita et. al. (Nivedita et al., 2017) aimed to reveal Dean flow dynamics and their instabilities in low aspect ratio spiral microchannels at Reynolds numbers greater than 100. Later, Mehrdel et al. (Mehrdel et al., 2018) proposed a novel variable radius spiral-shaped micromixer for the enhancement of mixing over Reynolds numbers ranging from 0.1 to 10. This micromixer was modified by adding the expansion and contraction sections.

The application areas of spiral microchannels have been extended during recent years due to their advantages in inducing chaotic advection in the laminar flow regime, which is the common flow regime in microscale, for applications such as particle separation (Bhagat et al., 2008), synthesis of micro-nano structures (Hao et al., 2019; Nie et al., 2017) and cell separation (Guzniczak et al., 2020; Sun et al., 2012). Recently, Erdem et. al. (Erdem et al., 2020) studied differential sorting of microparticles with different sizes in spiral microchannels having elliptic configurations. Focusing of fluorescent microparticles in the proposed channel was examined in microchannel configurations with a varying radius of curvature at different Reynolds numbers.

Motivated by the abovementioned studies, in this study, we present a new class of spiral microchannels having elliptic structures with different initial aspect ratios and curved serpentine microchannels with different numbers of baffles and baffle geometries for enhanced mixing. The channel designs of spiral elliptic micromixers (M1 to M4) were based on the past study (Erdem et al., 2020), which focused on the differential sorting of microparticles. The effect of the varying curvature radius of the elliptic spiral geometry on the mixing performance is displayed by calculating the mixing indices in different sections along the microchannel at Reynolds numbers ranging from 10 to 100.

Besides, according to the study conducted by Alijani et.al. (Alijani et al., 2019), the micromixer consisted of ten arcs of 280° curve angle have the optimum mixing performance. Here, seven curved serpentine micromixers with curvature angles of 280° (M1 to M7) were designed, each possessing six mixing segments. In particular, three different baffle configurations including quasi-rectangular, forward triangular, and backward triangular were structured. It was expected that the baffles would generate local small vortices in the laminar flow (Alam et al., 2014; Santana et al., 2019), which would enhance the mixing of the two fluids at relatively low Reynolds numbers (<50). Also, these baffles can enhance the mixing performance by agitating the flow (Bazaz et al., 2018). In this regard, the mixing capability of each micromixer was obtained by the mixing indices along the longitudinal length of the micromixers at Reynolds numbers 1 to 50.

1.2. Thesis Outline

In the dissertation, two types of micromixers are presented. They have elliptic spiral and curved serpentine microchannel geometries. Elliptic spiral microchannels have a varying radius of curvatures due to the ellipse-shaped geometry. The initial aspect ratios, the ratio of the distance of origin to the x- and y-axis, of the four microchannels vary as 3:2, 11:9, 9:11, and 2:3 for M1, M2, M3, and M4 micromixers, respectively. The width and height of the elliptic spiral microchannels are 500 μm and 70 μm, respectively.

Curved serpentine micromixers have six segments and 280° curvature angle with 500 μm inner radius of curvature of the inner arcs, 300 μm width, and 100 μm height. The number of baffles and baffle geometries vary for seven different micromixers as quasi-rectangular, forward triangular, and backward-triangular baffles which are embedded on the wall of the microchannels. For comparison, the first micromixer, M1 does not have any baffle geometry. Accordingly, there are five baffles in each curve within micromixers M2, M4, and M6, while there are eight baffles within micromixers M3, M5, and M7.

The presented PDMS (polydimethylsiloxane) micromixers were fabricated using a standard soft lithography technique without using any multilayer alignment. The mixing performance of the proposed micromixers was revealed by quantitively and qualitatively analyzing the path line of the Diluted Rhodamine B solution and DI water streams using an inverted fluorescence microscope. The fabrication and the experimental procedures are mainly similar for elliptic spiral and curved serpentine micromixers. Thus, these procedures are explained in the same chapter by revealing the differences in the processes.

In Chapter 2, the details of the micromixers' designs are presented separately. Besides, the fabrication and experimental procedures and mixing performance analysis which are common for both micromixers are explained. Also, the theory based on the utilization of Dean vortices and Dean flows, which occur due to the curved geometry of the proposed microchannels, is provided.

In Chapter 3 and Chapter 4, the results, discussions, and concluding remarks are presented separately for elliptic spiral and curved serpentine micromixers.

CHAPTER 2.

DESIGN, MATERIALS AND METHODS

2.1. Micromixer Design

2.1.1. Spiral Elliptic Micromixers

The spiral elliptic micromixers in this study have five-loop spiral designs with a width of 500 µm (W), a height of 70 µm (H), accordingly an aspect ratio of 0.14 (H/W). The total length of the ellipse-shaped microchannels is approximately 43 cm. The distance between each loop is fixed as 500 µm. Fluid streams are introduced to the micromixers from two inlets which are located at the center of the microchannels. Micromixers have an elliptic configuration with different initial aspect ratios (IAR), the ratio of the distance of the origin to the x and y-axis: 12:8(3:2), 11:9, 9:11, 8:12(2:3) (Figure 1). The channel orientations in the cartesian coordinate system differ for each micromixer. The M1 and M2 mixers have a wider part on the x-axis, whereas the wider parts of the M3 and M4 mixers are located on the y axis.

The radii of the initial loop of the mixers on the x and y-axis are represented as r_x and r_y (Table 1). The radius of curvature at thirteen different locations along the elliptic micromixers (Figure 1.a) is calculated according to the maximum and minimum radius of curvature formula as displayed in Table 1. Also, in Figure 1.a, the vertical distance between the sections located on the y-axis and the origin of the microchannel is demonstrated as v.l. (vertical length).

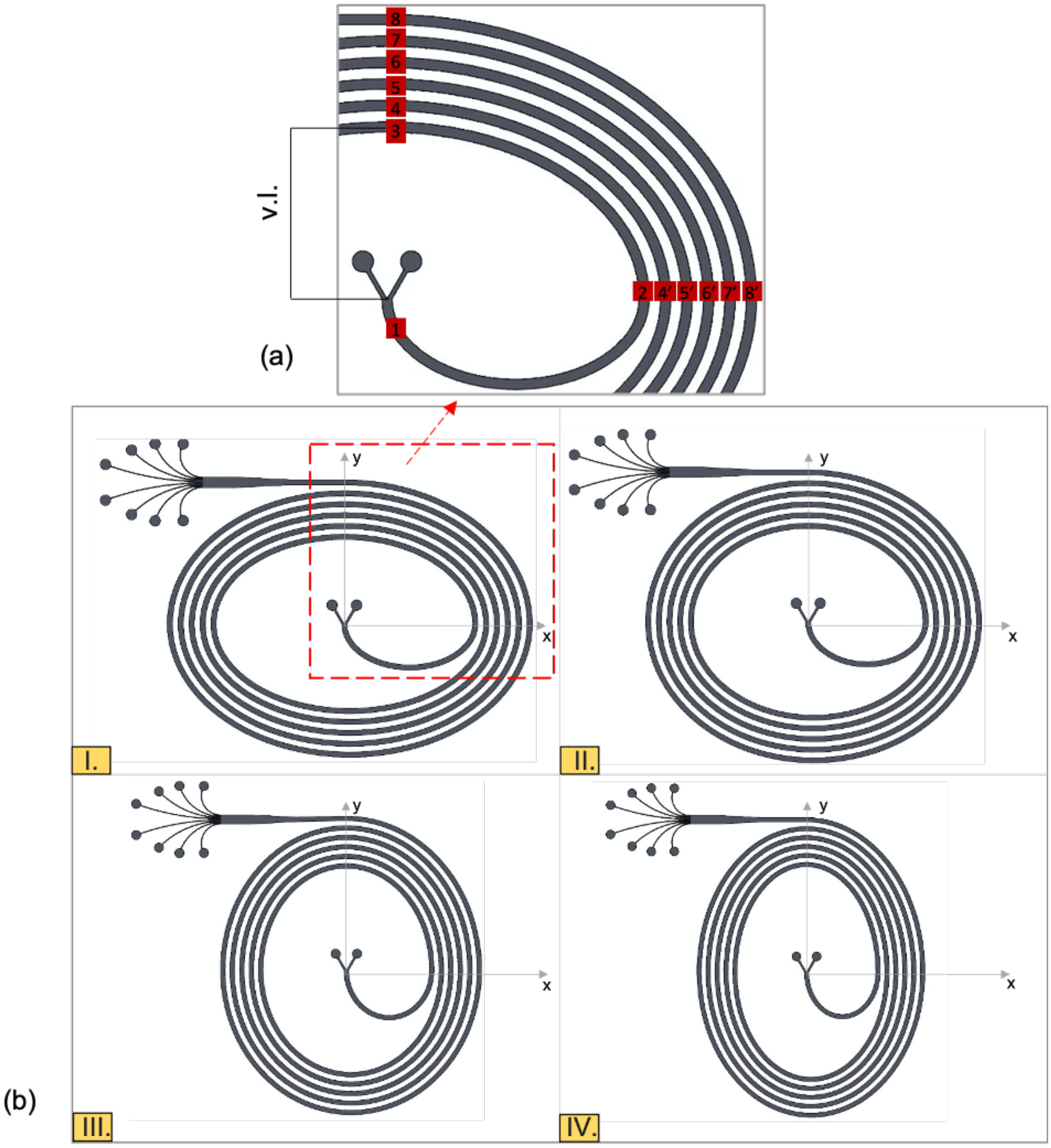

Figure 1. The schematic drawing of micromixers **(a)** The locations on the micromixers, where Dean numbers are calculated. The radius of curvature values at these locations are substituted into the Dean number formula. "v.l." represents the vertical length, which is the distance between the sections located on the y-axis and the origin of the microchannel in millimeters. **(b)** The schematic representation of micromixers having different elliptic configurations on a cartesian coordinate system. (I): M1 (IAR: 3:2), (II): M2 (IAR: 11:9), (III): M3 (IAR: 9:11), (IV): M4 (IAR: 2:3).

Table 1. The common and initial geometrical parameters for all micromixers. The maximum and minimum radius of curvature values stand for the channel curvature radius at second and third locations (Modified with permission from the study of Erdem et. al. (Erdem et al., 2020)).

Initial Geometrical Parameters

	Channel Height (μm)	Channel Width (μm)	r_x (mm)	r_y (mm)	Initial Aspect Ratio (IRA)	Maximum Radius of Curvature, R_{max} (mm)*	Minimum Radius of Curvature, R_{min} (mm)**
M1			12	8	3:2	18.0	5.3
M2	70	500	11	9	11:9	13.4	7.4
M3			9	11	9:11	13.4	7.4
M4			8	12	2:3	18.0	5.3

$*R_{max} = \max\left(\frac{r_x^2}{r_y}, \frac{r_y^2}{r_x}\right)$ and $**R_{min} = \min\left(\frac{r_x^2}{r_y}, \frac{r_y^2}{r_x}\right)$

In regular spiral channels, the radius of curvature increases linearly due to the fixed center of curvature. Thus, a subsequent decrease in the intensity of secondary flow is observed along the channel. However, in elliptic spiral microchannels, the center of curvature changes because of the ellipse-shaped geometry. Due to the varying radius of curvature along the micromixers and the change in centrifugal forces along each quarter loop, Dean vortices and Dean flow profiles vary at different locations in these microchannels. To study the effect of varying radius of curvature in the channels, the corresponding Dean values were calculated at the indicated locations in Figure 1a. Moreover, after the eight locations depicted in Figure 1b, the width of the channel increases from 500 μm to 1000 μm at the straight part of the channel (ninth section). The effect of the expansion of the channel width on the mixing performance was observed in the proposed micromixers.

2.1.2. Curved Micromixers with Various Baffle Geometries

The effect of curvature angle on mixing in curved serpentine micromixers was investigated in the study conducted by Alijani et. al. (Alijani et al., 2019). Accordingly, the higher curvature angle leads to a higher mixing efficiency at lower Reynolds numbers. The obtained results are utilized in this study. The mixing performance is aimed to be enhanced by introducing baffles into the sidewalls of the micromixers with a higher curvature angle (i.e., 280°). Due to the fabrication limitations, the micromixers having curvature angle beyond the 280° could not be used. As it is reported in the previous study, for curve angles close to 360°, the curves contact each other (Alijani et al., 2019).

The inner radius of curvature of the inner arcs is 500μm, and the width and height of the micromixers are 300 μm and 100 μm, respectively. Three different baffle configurations including quasi-rectangular, forward triangular, and backward triangular are designed. Table 2 includes the geometrical parameters of the micromixer designs. The width of the baffles in all designs is kept as 150μm, which is half of the micromixers' widths. As Figure 2 shows, all the micromixers consist of six mixing segments. Accordingly, there are five baffles in each curve in micromixers M2, M4, and M6, while there are eight baffles in micromixers M3, M5, and M7. It is expected that the baffles generate local small vortices in the laminar flow, which enhances the mixing of two fluids (Alam et al., 2014; Santana et al., 2019). Also, Figure 2 displays the location of the inlets of the two streams, where the main flow direction is from left to right.

Table 2. Summarized designs of micromixers

Geometric Parameters				
Micromixer types	Baffle geometry	Baffle Width (μm)	Baffle length $\boldsymbol{\theta}_b$ (degrees)	Baffle spacing $\boldsymbol{\theta}_s$ (degrees)
M1	-	-	-	-

M2	Quasi-rectangular	150	14	42
M3	Quasi-rectangular	150	8.75	26.25
M4	Forward triangular	150	14	42
M5	Forward triangular	150	8.75	26.25
M6	Backward triangular	150	14	42
M7	Backward triangular	150	8.75	26.25

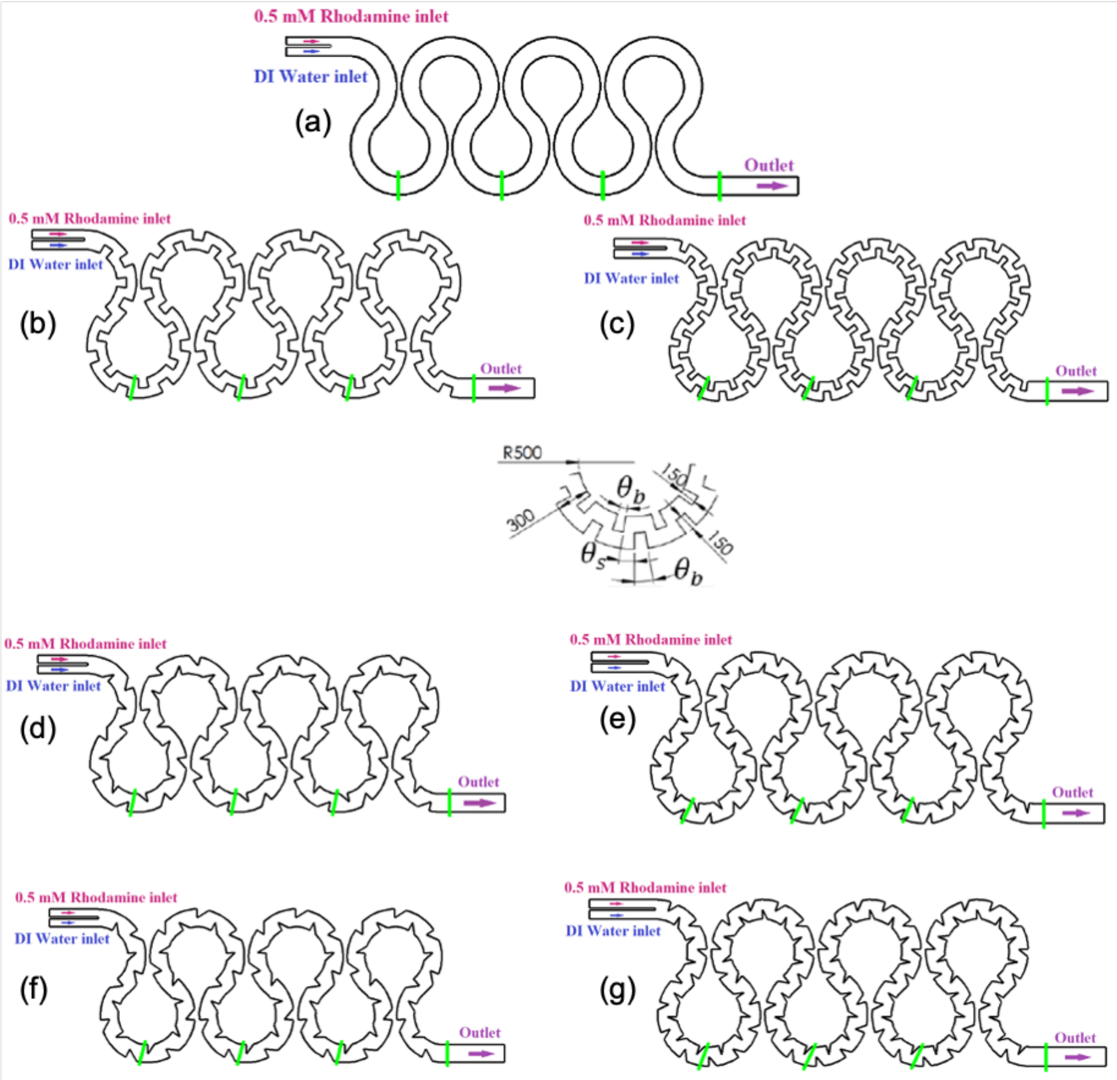

Figure 2. The schematics of **(a)** M1, **(b)** M2, **(c)** M3, **(d)** M4, **(e)** M5, **(f)** M6, **(g)** M7 micromixers. The green lines demonstrate the location of evaluated mixing indices over the channel length.

2.2. Theory

Turbulent effects are desired for rapid mixing in macro-scale systems. However, in microchannels, the laminar flow regime is mostly observed due to the small size and flow velocity. The dimensionless Reynolds number, *Re*, is a key parameter and is the ratio of the fluid inertia to viscous forces:

$$Re = \frac{\rho U D_h}{\mu} \tag{1}$$

where $\rho,\ U,\ D_h$, and μ represent the fluid density (kg/m^3), average flow velocity (m/s), microchannel hydraulic diameter (m), and fluid dynamic viscosity (kg/m.s), respectively. The hydraulic diameter of the proposed microchannels having a rectangular cross-section is calculated from the below equation:

$$D_h = \frac{2ab}{(a+b)} \tag{2}$$

where *a* and *b* represent the microchannel cross-sectional dimensions (m).
Moreover, the mixing time (s) is defined as (Karnik, 2008):

$$t_{mix} \sim \frac{l_{st}^2}{D} \tag{3}$$

where l_{st} indicates the striation length (m) and D is the diffusivity of the species (m^2/s). Accordingly, rapid mixing can be achieved by decreasing the striation length known as the distance along which diffusion occurs. Stretching and folding the fluid in the channel constitute an approach to reduce the striation length while enlarging the surface area for diffusion. The other important dimensionless number, Péclet number , *Pe*, number, is the ratio of the advective to diffusive transport and is defined as (Bayareh et al., 2020):

$$Pe = \frac{D_h U}{D} = \frac{advection\ transport}{diffusion\ transport} \tag{4}$$

Accordingly, mixing occurs due to the advection at Péclet numbers larger than 1. Conversely, for Pe smaller than 1, diffusion dominates the mixing process (Rapp, 2017). In this study, the smallest Pe number of the spiral elliptic micromixers is calculated as 2.77×10^4 for a hydraulic diameter of 122.8 μm, the lowest flow rate of 0.171 mL/min, and the diffusivity of Rhodamine B in the water of 3.6×10^{-10} m^2 / s (Rani et al., 2005). Similarly, the smallest Pe number of the serpentine micromixers with baffle geometries is greater than the critical value 1 for the hydraulic diameter of 150 μm, the lowest flow rate of 0.012 mL/min, and the diffusivity of Rhodamine B in water. Thus, the mixing is governed by advection rather than diffusion, which is achieved by the curved geometry of the channels. The occurrence of chaotic advection by the presence of Dean vortices and secondary flow provides an enhancement in mixing. Accordingly, the radius of curvature of the microchannel geometry provides the formation of secondary flows, which form due to the non-linear centrifugal forces acting on the working fluid. The fluid molecules at the center move to the outer part and then come back to the center of the channel. Two counter-rotating vortices occur with the recirculation of fluid, and this double vortex known as Dean vortices occurs perpendicular to the original flow and allows fluid to move to upward and downward directions in the microchannel (Alijani et al., 2019; Chen et al., 2011; Dean & Hurst, 1959; Erdem et al., 2020; Nivedita et al., 2017; Sudarsan & Ugaz, 2006). Thus, mixing is achieved by stretching and folding the interface of the liquid streams (Duryodhan et al., 2017). The formation of Dean vortices and magnitude of the Dean flow is represented by the dimensionless Dean number (Akgönül et al., 2017):

$$De = Re\sqrt{\delta} = Re\sqrt{\frac{D_h}{2R}} \tag{5}$$

where R is the radius of curvature of the microchannel and δ represents the ratio of the channel hydraulic diameter to the microchannel radius of curvature.

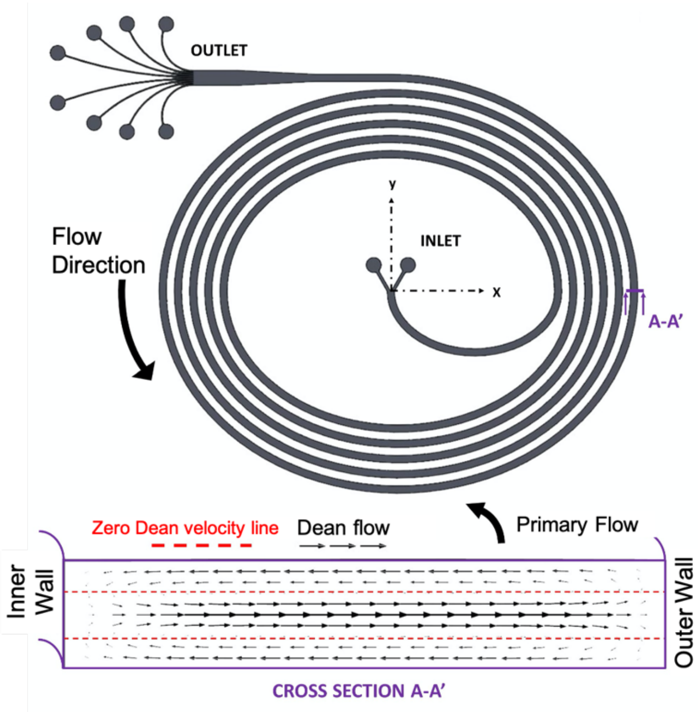

Figure 3. Illustration of Dean flow effect in the elliptic spiral microchannel at the segment denoted as A-A.

Figure 3 demonstrates the effect of Dean flow in the elliptic spiral microchannels with the presence of Dean vortices. The fluid at the center, which has a larger velocity, tends to move to the near-wall region of the channel due to the inertia, which causes a pressure gradient and recirculation of fluid (Di Carlo, 2009). The transverse motion of the flow leads to the generation of Dean vortices and Dean flow, which enhance the mixing performance by stretching, folding, and breaking up the fluid.

2.3. Microchannel Fabrication

2.3.1. Fabrication Materials

The fabrication of the PDMS (polydimethylsiloxane) microchannels was completed using the master silicon wafers (University Wafer, Inc., Boston, MA, USA). According to the size of the acetate masks represented in Figure 4 and Figure 5, the 3'' and 4'' silicon wafers were chosen for elliptic spiral and curved serpentine microchannels respectively.

The 2D acetate masks of the elliptic spiral and curved serpentine were provided from Çözüm Baskı Center and CAD/Art Services, Inc., accordingly. The negative photoresist of SU-8 3050, which has a photoresist coating thickness up to 100 µm, and specific developer of SU-8 3050 were provided by MicroChem Corporation. The fabrication was completed at the ISO class 2 cleanroom facility of Sabanci University Nanotechnology Research and Applications Center (SUNUM). The spinner and hot plates were provided by Dorutek-Lithography-Wet-Bench, and Ultraviolet-Lithography device MDA-60MS Mask Aligner 4'' was supplied by Midas System Co. The molding of the microchannels was done by the PDMS prepolymer base and curing agent which were provided by Sylgard 184 silicone elastomer kit by Dow Corning. To eliminate the bubble formations in the PDMS mixture and baking the PDMS, a heater-integrated vacuum chamber by Sheldon Manufacturing, Inc. was utilized. As a final step, the oxygen plasma device of Harrick Plasma Cleaner was employed for the bonding of PDMS microchannels and glass slides.

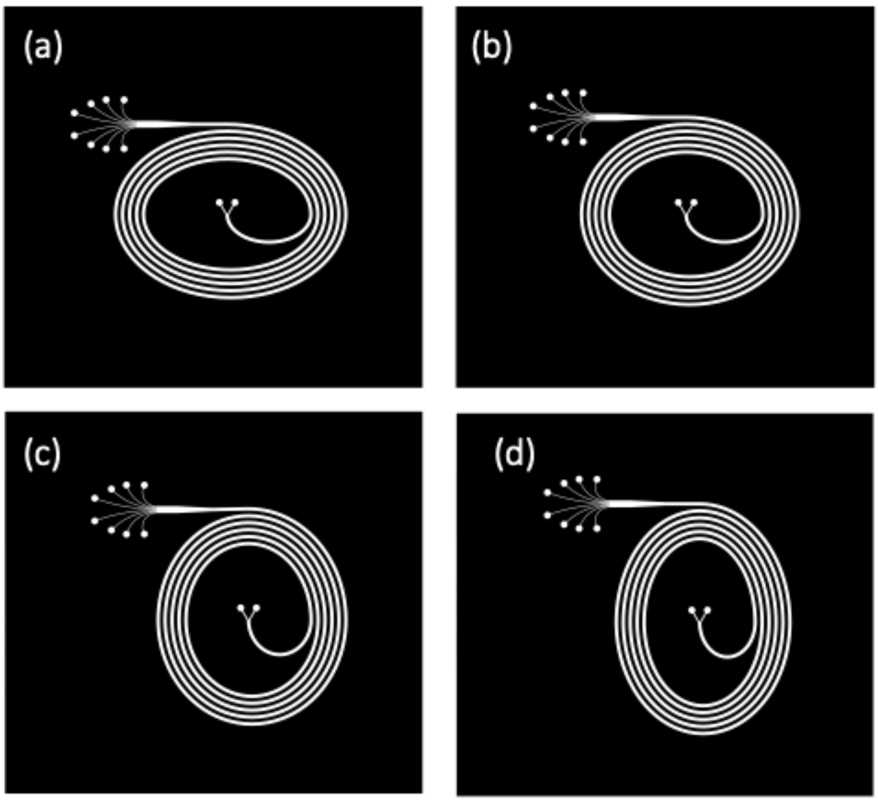

Figure 4. The 2D acetate mask designs of **(a)** M1, **(b)** M2, **(c)** M3, **(d)** M4 microchannels.

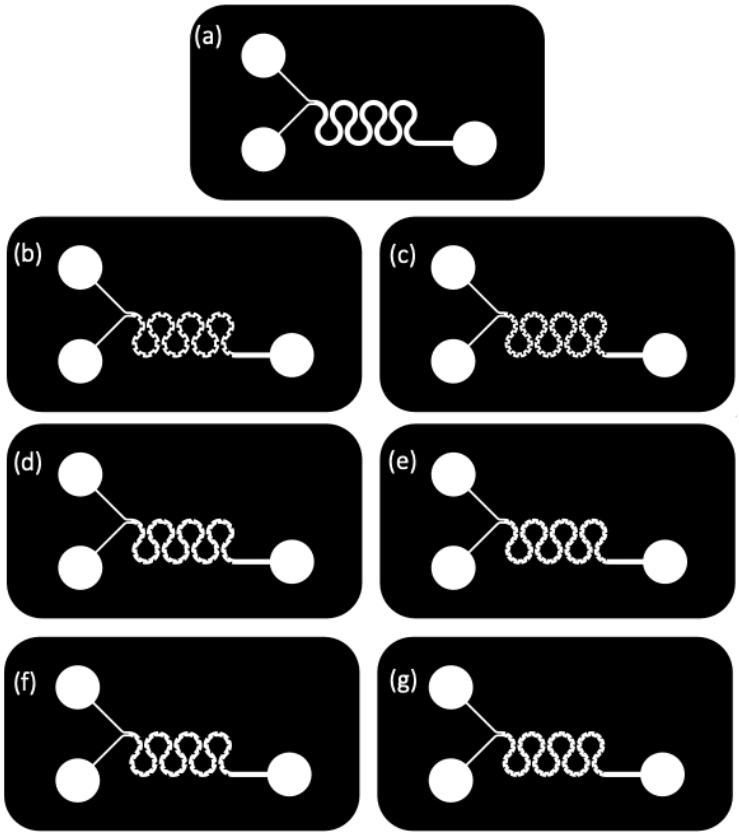

Figure 5. The 2D acetate mask designs of **(a)** M1, **(b)** M2, **(c)** M3, **(d)** M4, **(e)** M5, **(f)** M6, **(g)** M7 microchannels.

2.3.2. Fabrication Procedure

The fabrication of the elliptic spiral and curved serpentine microchannels were done by a single step lithography process without using any multilayer alignment at the ISO class 2 cleanroom facility of Sabanci University Nanotechnology Research and Applications Center (SUNUM). All stages of the processes were the same for both microchannel designs except the spin coating step which the photoresist coating thickness of 70 µm and 100 µm were achieved for elliptic spiral and curved serpentine microchannels accordingly. A polished side of the 3" and 4'' silicon wafers were used to prepare master wafers for the PDMS molding process for elliptic spiral and curved serpentine microchannels, respectively.

Initially, the sample preparation was achieved by washing the wafer with isopropyl alcohol (IPA) and dried with Nitrogen gas (N_2) to eliminate the dust. According to the parameters of the negative photoresist SU-8 3050 which are provided by the MicroChem Corporation in Figure 6, the spin coating process was arranged by computer-controlled spin coater to have a uniform distribution of the photoresist on the wafer surface. To obtain a photoresist coating thickness of ~ 70 µm for the elliptic spiral microchannels, the spinner program consisted of three steps was set initially to 500 rpm for 10 seconds then 1900 rpm for 30 seconds and lastly, the wafer was rest for five seconds before opening the spin coater due to the high viscosity feature of SU-8 to protect the wafer from dripping. Similarly, the photoresist coating thickness of ~100 µm was obtained by three steps spinner program which include initially 500 rpm for 10 seconds then 1000 rpm for 30 seconds and lastly, five seconds rest for curved serpentine microchannels.

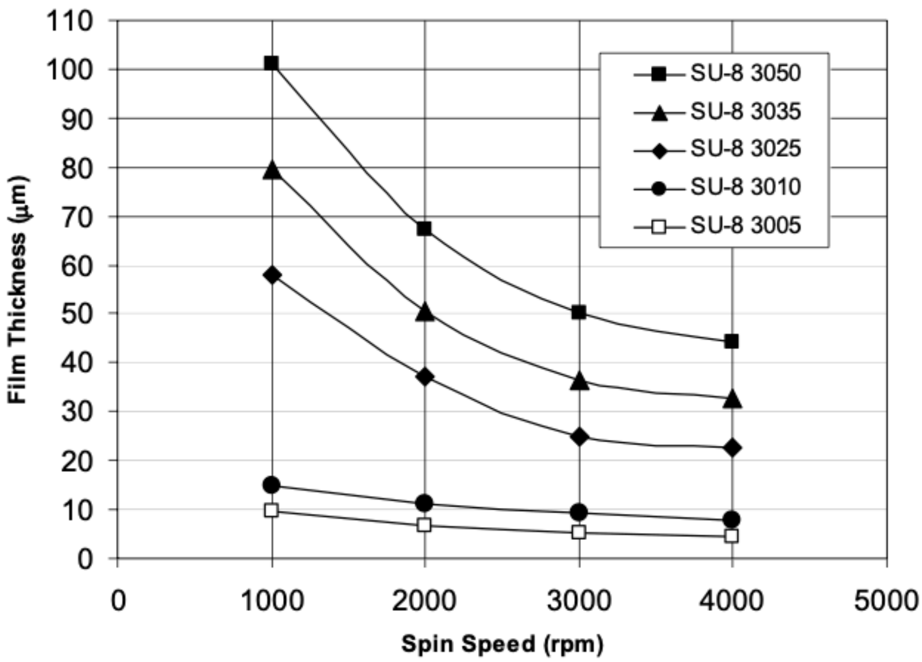

Figure 6. The film thickness of the SU-8 3000 resists vs. the spin speed (21°C US & EU) provided by MicroChem Corporation (Microchem, 2000).

The wafer was placed at the center of the wafer holder of the spin coater and vacuumed to prevent displacement during the coating process. Then the SU-8 3050 was dispensed at the center of the 3'' and 4'' wafer surfaces with the amount of 3 ml and 4 ml for elliptic spiral and curved serpentine microchannels, respectively. Then, the spin coater was activated to achieve the desired thickness of the negative photoresist with the predefined spinning program.

The hot plate at 95 °C was used for the soft bake step and the wafer was kept for 15 minutes on the hot plate. Then, it was left to cool at room temperature after ensuring that there is no wrinkle on the wafer surface. The soft bake procedure followed a photolithography step in which the SU-8 coated silicon wafer was placed at the center of the wafer holder of the Mask Aligner UV Lithography device. The acetate masks were stuck on a rectangular glass slide by two-sided tapes and centered at the mask holder. The mask vacuum was opened, and it was placed on the UV Lithography device. After being sure that the mask and wafer were aligned, the 12 seconds of UV exposure was initiated to transfer the desired amount of exposure energy to obtain relevant patterns on the silicon wafer.

The post-exposure bake (PEB) step was set directly after the exposure which the wafer first baked at 65 °C for one minute and subsequently at 95 °C for five minutes. During this time, the patterns on the silicon wafer became visible. The unexposed areas were developed by immersing the silicon wafer in the petri dish filled with SU-8 developer (Microchem Corp.) for 8 minutes. After 8 minutes of controlled developing step, it was washed with SU-8 developer and IPA for approximately 10 seconds and was dried with N_2. As a final step, the silicon wafer was cured at 150 °C on a hot plate for 10 minutes to make sure that the material was cross-linked. The schematic representation of the master wafer fabrication process flow is represented in Figure 7.

All the specifications mentioned during the single-step lithography process such as soft bake and post bake durations, exposure and development time, and exposure energy were set according to the specifications presented by Microchem Corporation which are represented in Table 3.

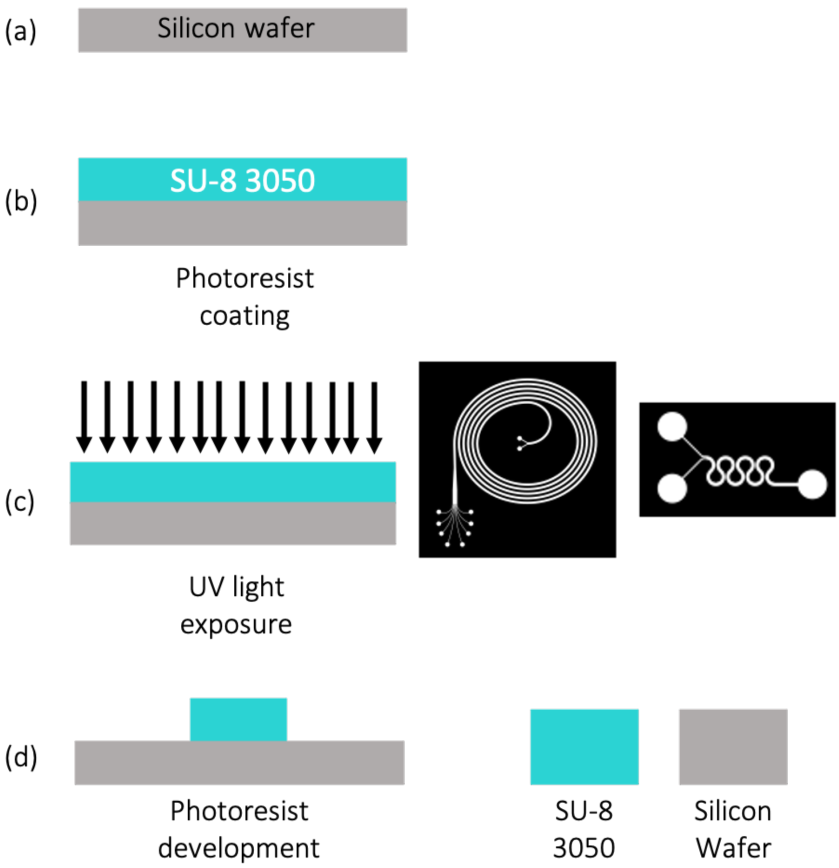

Figure 7. The schematic representation of the fabrication process flow.

Table 3. Specifications of the SU-8 3050 negative photoresist provided by Microchem Corporation.

Process Specifications of SU-8 3050 Resist					
Thickness (µm)	Soft Bake Duration (min)	Exposure Energy (mJ/cm^2)	PEB Time (65 °C) (min)	PEB Time (95 °C) (min)	Development Duration (min)
40 – 100	15 – 45	150 – 250	1	3 – 5	7 - 15

The fabricated master wafers were utilized to obtain polydimethylsiloxane microchannels. For this purpose, the PDMS solution was prepared by manually well stirred the PDMS prepolymer base and curing agent which were arranged in the ratio of 10:1 using the assay balance scale. The mixture was poured into the glass petri dish, where the master silicon wafer was placed. A heater-integrated vacuum chamber under 76 mTorr was used to degas the PDMS mixture, which has bubble formations due to the mixing, for half an hour until there was no bubble observed in the mixture. After the degassing, the vacuum was closed, and the chamber temperature set to 110 °C and petri dishes filled with PDMS mixture were left for 1.5 hours for the hardening.

Thereafter, the baked PDMS was carefully separated from the master wafer by cutting the desired part in a rectangular shape which encloses the microchannel by using a scalpel. A 21-gauge needle with sharpened tips was used for the opening of the inlet and outlet holes. Next, the PDMS microchannels and glass slides which will be used in the bonding process were washed with (IPA) and blow-dried by N_2 gas. The surface of the PDMS microchannel was covered by tape to prevent the undesired dust and dirt.

The final step of the fabrication was completed by bonding the PDMS microchannel on the glass slide using an oxygen plasma device. Before the process, the tape on the surface of the PDMS microchannel was removed. The microchannel was placed into the plasma chamber with a glass slide where the PDMS microchannel was faced up to provide the plasma activation of the patterned surface. Under vacuum condition, the plasma was opened in a high radio frequency setting and the periodic infusion of O_2 every 10 seconds with 10 ml/min dose was subjected for 60 seconds. Then, the vacuum condition was eliminated by supplying the air into the chamber. The microfluidics devices were formed directly after opening the chamber by gently pressing the plasma-treated PDMS surface on the glass slide.

2.4. Mixing Materials and Experimental Setup

2.4.1. Mixing Materials

Diluted Rhodamine B solution and DI water were used during the experiments. The fluorescence solution was prepared by solving 0.024 gr of Rhodamine B powder (Merck KGaA, Darmstadt, Germany) in 100 mL DI water. The uniform distribution of the mixture was obtained by mixing the solution for 15 minutes with a magnetic stirrer.

2.4.2. Experimental Equipment and Procedure

The experimental equipment and procedures are the same for both micromixer types which were carried out by extracting the intensity profiles of the fluid flow in the microchannels. An inverted fluorescence microscope (ZEISS Axio Observer Z1 Live Cell Imaging) was utilized for qualitative and quantitative analysis of mixing (Figure 8). The visualization of the mixing process of elliptic spiral microchannels was achieved by taking snapshots of the fluid flow at nine different locations along the microchannels which are shown in Figure 9. For the curved serpentine micromixers, the whole picture of the microchannel is taken by dividing it into eight tiles and thereby combining them into one image.

The flow rates were set by plastic syringes which were installed to the dual syringe pump (LEGATO® 200, KD Scientific, Holliston, MA, USA). TYGON tubings with 250 μm internal diameter (IDEX Corp., Lake Forest, IL, USA) and metal fittings (IDEX Corp.) were used to pump the liquids from the syringes to the inlet of the channel and from the outlet of the channel to the reservoir. For elliptic spiral microchannels, the flow rates varying from 0.171 to 1.71 mL/min ($10 \leq Re \leq 100$) were set by using two 20 mL plastic syringes whereas the flow rates from 0.012 to 0.6 mL/min ($1 \leq Re \leq 50$) were set for curved serpentine micromixers by using two 60 mL plastic syringes.

After the flow reaches the steady-state condition, the syringe pump was set to the minimum flow rate, and the image of the micromixer was taken. Then, the flow rate was increased, and images were taken after a 5-minute waiting time when there is no noticeable change in the flow field to ensure that the steady-state conditions were reached. This process was repeated until the maximum value of the flow rate, which corresponded to the Reynolds numbers 50 and 100 for curved serpentine and elliptic spiral microchannels, respectively.

(a) (b)

Figure 8. The images of the microfluidics platforms of **(a)** elliptic spiral and **(b)** curved serpentine micromixers on the experimental device. The Rhodamine B solution and water are introduced to the PDMS microchannels from the inlet parts (at the middle for the elliptic spiral microchannels and on the right for the curved serpentine micromixers).

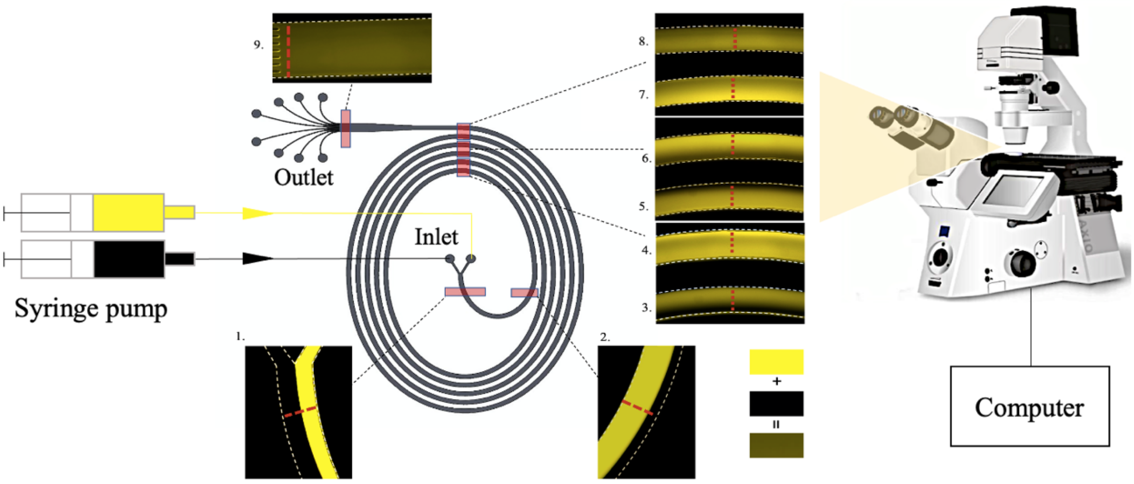

Figure 9. The schematic representation of the experimental setup. The nine sections at which the mixing indices of elliptic spiral micromixers are calculated is presented. The first section is the location near the inlet, and the ninth section is the one at the outlet. The yellow and black streams are denoted as the diluted Rhodamine B solution and DI water, respectively. The dark green color indicates the mixture. Images taken from

different locations are shown in zoom-in frames as an example. Red lines indicate the points of interest where the intensity values were taken for elliptic spiral microchannels.

2.5. Mixing Performance Analysis and Image Processing

The fluorescence images with 968 × 728 pixels were analyzed using microscope software (ZEN Blue 3.1) for both elliptic spiral and curved serpentine micromixers. The intensity versus distance profiles were extracted along the red lines and green lines depicted in Figure 9 and Figure 2, respectively. The length of the plotting line has a variation of 3-4 pixels from each side. Thus, the uncertainty is approximately 4% when proportional to the number of pixels corresponding to the microchannel width. The data set was used to calculate the mixing index (*M*) defined as (Alijani et al., 2019):

$$M = 1 - \sqrt{\frac{1}{N}\sum_{i=1}^{N}\left(\frac{I_i - \bar{I}}{\bar{I}}\right)^2} \tag{6}$$

where N, I_i and $\bar{I}$ represent the number of pixels, the fluorescence intensity of the ith pixel, and the average fluorescence intensity of all pixels, respectively. Accordingly, perfect mixing occurs at the value of the mixing index equal to one, whereas the value of zero suggests no mixing.

CHAPTER 3.

RESULTS AND DISCUSSION

3.1. Spiral Elliptic Micromixers

3.1.1. The variation of Dean numbers along the micromixers

The radius of curvature increases linearly in regular spiral channels because of the fixed center of the curvature. However, the curvature center differs along the elliptic channels, which causes a varying curvature radius and unsteady Dean numbers in the microchannel. Figure 10 shows an example of the variation of Dean numbers along with the M1 micromixer for the Reynolds numbers, *Re*= 10, 30, 100. Table 4-Table 7 represents the corresponding Dean numbers and Table 8 shows the radius of curvatures along with the M1, M2, M3, and M4 microchannels at different sections for Reynolds numbers ranging from 10 to 100. For the M1 and M2 mixers, the maximum radius of curvature is located on the y axis, whereas the minimum radius of curvature is located on the x-axis. Consequently, Dean numbers decrease by moving from a point on the x-axis to the next point on the y axis and then increase by moving from a point on the y-axis to the next point on the x-axis Figure 10.

For the M3 and M4 micromixers, the maximum radius of curvature is located on the opposite axis. Thus, Dean numbers increase by moving from the point on the x-axis to the following point on the y axis (i.e., from point 4’ to 4) and then decrease by moving from the points on the y-axis to the x-axis (i.e., from point 4 to 5’). Due to the increase in the radius of curvature, while moving from the first loop to the last loop, the strength of Dean flow along the micromixers decreases. Also, as expected from Eq. 5, the Dean number gradually increases with the higher Reynolds numbers.

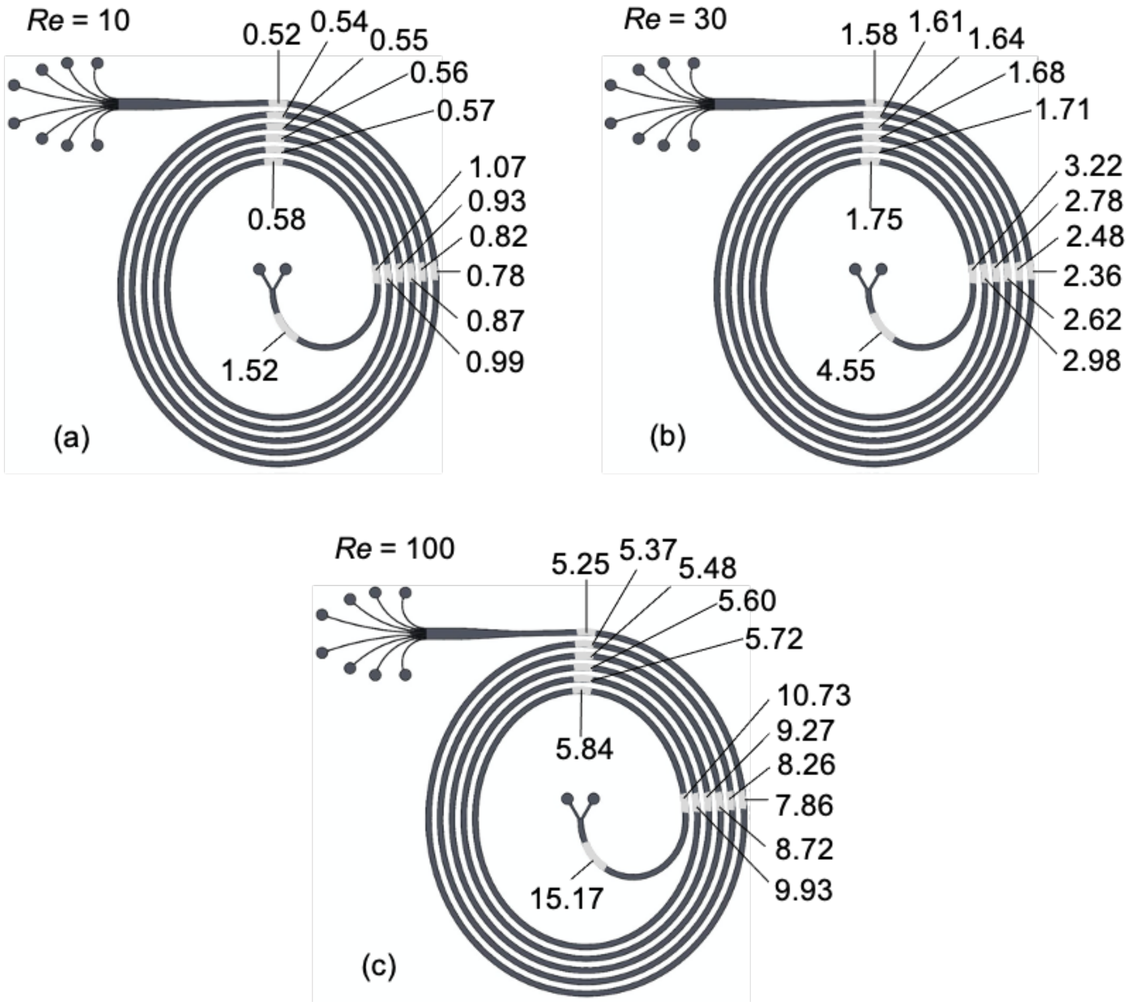

Figure 10. Variation of Dean number at different sections along the M1 micromixer according to the radius of curvatures at Reynolds numbers. **(a)** *R*e = 10, **(b)** *Re*= 30, **(c)** *Re*= 100.

It is worthwhile to mention that as the Reynolds number increases, the Dean number increases linearly at the first (inlet) section of the micromixers. For the following sections, as seen in Figure 10, a fluctuating trend in Dean number values, decrease and increase, is observed along the microchannel. Even though the Dean number values are smaller near the outlet section compared to the previous sections, an efficient mixing rapidly occurs at the last sections of the micromixers at *Re*<40, which shows the dominant effect of unbalanced Dean numbers on enhancing the mixing performance.

Table 4. Corresponding Dean numbers at different sections along the M1 microchannel for Reynolds numbers ranging from 10 to 100)

		Section numbers												
		1	**2**	**3**	**4'**	**4**	**5'**	**5**	**6'**	**6**	**7'**	**7**	**8'**	**8**
Re	**10**	1.52	1.07	0.58	0.99	0.57	0.93	0.56	0.87	0.55	0.83	0.54	0.79	0.53
	20	3.03	2.15	1.17	1.99	1.14	1.85	1.12	1.74	1.10	1.65	1.07	1.57	1.05
	30	4.55	3.22	1.75	2.98	1.72	2.78	1.68	2.62	1.64	2.48	1.61	2.36	1.58
	40	6.07	4.29	2.34	3.97	2.29	3.71	2.24	3.49	2.19	3.30	2.15	3.14	2.10
	50	7.59	5.36	2.92	4.96	2.86	4.64	2.80	4.36	2.74	4.13	2.68	3.93	2.63
	60	9.10	6.44	3.50	5.96	3.43	5.56	3.36	5.23	3.29	4.96	3.22	4.72	3.15
	70	10.62	7.51	4.09	6.95	4.00	6.49	3.92	6.11	3.84	5.78	3.76	5.50	3.68
	80	12.14	8.58	4.67	7.94	4.57	7.42	4.48	6.98	4.38	6.61	4.29	6.29	4.20
	90	13.66	9.66	5.26	8.93	5.15	8.34	5.04	7.85	4.93	7.43	4.83	7.07	4.73
	100	15.17	10.73	5.84	9.93	5.72	9.27	5.60	8.72	5.48	8.26	5.36	7.86	5.26

Table 5. Corresponding Dean numbers at different sections along the M2 microchannel for Reynolds numbers ranging from 10 to 100)

		Section Numbers												
		1	**2**	**3**	**4'**	**4**	**5'**	**5**	**6'**	**6**	**7'**	**7**	**8'**	**8**
Re	**10**	1.29	0.91	0.68	0.86	0.65	0.81	0.63	0.77	0.61	0.74	0.60	0.71	0.58
	20	2.58	1.83	1.35	1.72	1.31	1.62	1.26	1.55	1.23	1.48	1.19	1.42	1.16
	30	3.87	2.74	2.03	2.58	1.96	2.44	1.90	2.32	1.84	2.21	1.79	2.12	1.74
	40	5.17	3.65	2.70	3.43	2.61	3.25	2.53	3.09	2.45	2.95	2.38	2.83	2.32
	50	6.46	4.57	3.38	4.29	3.27	4.06	3.16	3.86	3.07	3.69	2.98	3.54	2.90
	60	7.75	5.48	4.05	5.15	3.92	4.87	3.79	4.64	3.68	4.43	3.57	4.25	3.48
	70	9.04	6.39	4.73	6.01	4.57	5.69	4.43	5.41	4.29	5.17	4.17	4.96	4.06
	80	10.33	7.31	5.41	6.87	5.22	6.50	5.06	6.18	4.91	5.91	4.77	5.66	4.64
	90	11.62	8.22	6.08	7.73	5.88	7.31	5.69	6.95	5.52	6.64	5.36	6.37	5.22
	100	12.91	9.13	6.76	8.58	6.53	8.12	6.32	7.73	6.13	7.38	5.96	7.08	5.79

Table 6. Corresponding Dean numbers at different sections along the M3 microchannel for Reynolds numbers ranging from 10 to 100)

		Section numbers												
		1	**2**	**3**	**4'**	**4**	**5'**	**5**	**6'**	**6**	**7'**	**7**	**8'**	**8**
Re	**10**	0.96	0.68	0.91	0.65	0.86	0.63	0.81	0.61	0.77	0.60	0.74	0.58	0.71
	20	1.91	1.35	1.83	1.31	1.72	1.26	1.62	1.23	1.55	1.19	1.48	1.16	1.42
	30	2.87	2.03	2.74	1.96	2.58	1.90	2.44	1.84	2.32	1.79	2.21	1.74	2.12
	40	3.82	2.70	3.65	2.61	3.43	2.53	3.25	2.45	3.09	2.38	2.95	2.32	2.83
	50	4.78	3.38	4.57	3.27	4.29	3.16	4.06	3.07	3.86	2.98	3.69	2.90	3.54
	60	5.73	4.05	5.48	3.92	5.15	3.79	4.87	3.68	4.64	3.57	4.43	3.48	4.25
	70	6.69	4.73	6.39	4.57	6.01	4.43	5.69	4.29	5.41	4.17	5.17	4.06	4.96
	80	7.65	5.41	7.31	5.22	6.87	5.06	6.50	4.91	6.18	4.77	5.91	4.64	5.66
	90	8.60	6.08	8.22	5.88	7.73	5.69	7.31	5.52	6.95	5.36	6.64	5.22	6.37
	100	9.56	6.76	9.13	6.53	8.58	6.32	8.12	6.13	7.73	5.96	7.38	5.79	7.08

Table 7. Corresponding Dean numbers at different sections along the M4 microchannel for Reynolds numbers ranging from 10 to 100)

		Section numbers												
		1	**2**	**3**	**4'**	**4**	**5'**	**5**	**6'**	**6**	**7'**	**7**	**8'**	**8**
Re	**10**	0.83	0.58	1.07	0.57	0.99	0.56	0.93	0.55	0.87	0.54	0.83	0.53	0.79
	20	1.65	1.17	2.15	1.14	1.99	1.12	1.85	1.10	1.74	1.07	1.65	1.05	1.57
	30	2.48	1.75	3.22	1.72	2.98	1.68	2.78	1.64	2.62	1.61	2.48	1.58	2.36
	40	3.30	2.34	4.29	2.29	3.97	2.24	3.71	2.19	3.49	2.15	3.30	2.10	3.14
	50	4.13	2.92	5.36	2.86	4.96	2.80	4.64	2.74	4.36	2.68	4.13	2.63	3.93
	60	4.96	3.50	6.44	3.43	5.96	3.36	5.56	3.29	5.23	3.22	4.96	3.15	4.72
	70	5.78	4.09	7.51	4.00	6.95	3.92	6.49	3.84	6.11	3.76	5.78	3.68	5.50
	80	6.61	4.67	8.58	4.57	7.94	4.48	7.42	4.38	6.98	4.29	6.61	4.20	6.29
	90	7.43	5.26	9.66	5.15	8.93	5.04	8.34	4.93	7.85	4.83	7.43	4.73	7.07
	100	8.26	5.84	10.73	5.72	9.93	5.60	9.27	5.48	8.72	5.36	8.26	5.26	7.86

Table 8. Radius of curvatures at the different sections of the micromixers

Section no.	*Radius of curvature (mm)*			
	M1	**M2**	**M3**	**M4**
1	2.67	3.68	6.72	9.00
2	5.33	7.36	13.44	18.00
3	18.00	13.44	7.36	5.33
4'	6.23	8.33	14.40	18.78
4	18.78	14.40	8.33	6.23
5'	7.14	9.31	15.36	19.60
5	19.60	15.36	9.31	7.14
6'	8.07	10.29	16.33	20.45
6	20.45	16.33	10.29	8.07
7'	9.00	11.27	17.31	21.33
7	21.33	17.31	11.27	9.00
8'	9.94	12.25	18.29	22.23
8	22.23	18.29	12.25	9.94

3.1.2. Fluid mixing enhancement in elliptic micromixers

Figure 11 represents the mixing index for different section numbers of the micromixers which are shown in Figure 9 over the Reynolds numbers range, $10 \leq Re \leq 50$. Accordingly, the mixing index linearly increases by moving from the inlet to the outlet of the channel until $Re = 20$. A noticeable increase in mixing efficiency can be observed in the ninth section of the M4 micromixer with M from 0.48 to 0.82 as Re increases from 10 to 20 (Figure 11d). To better understand this change in the mixing performance, the two-fluid streams are examined in detail.

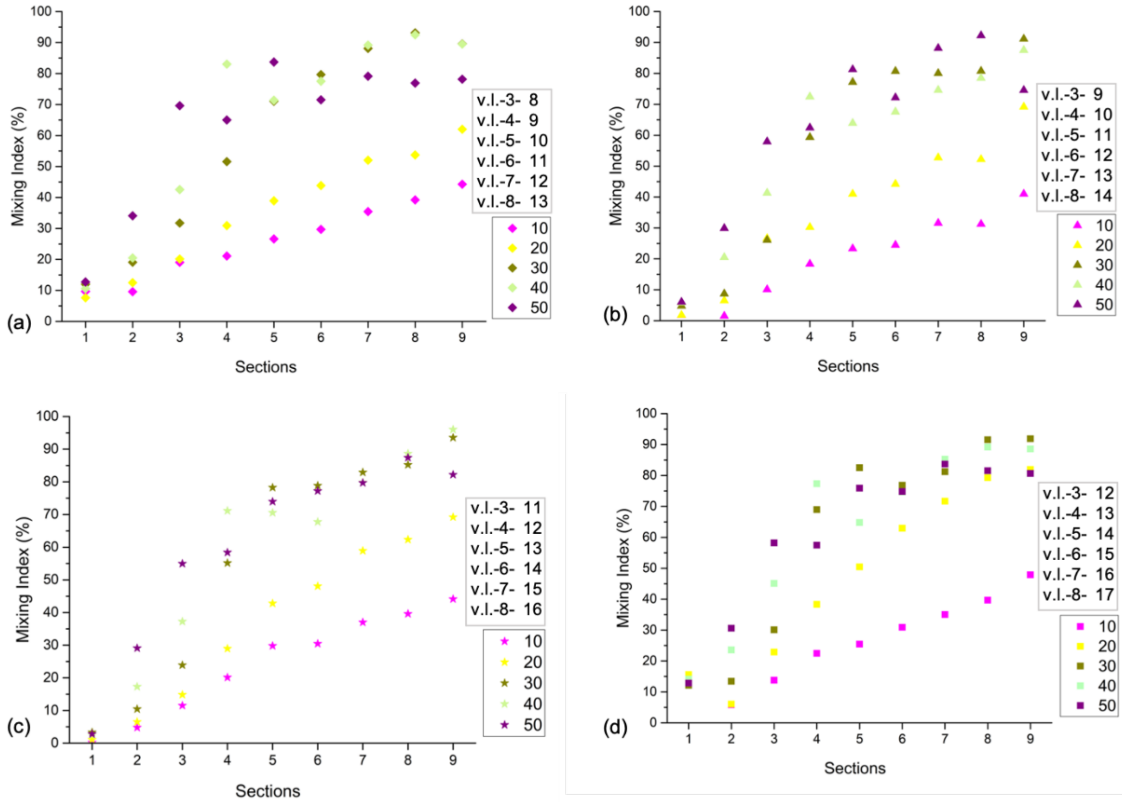

Figure 11. Mixing indices as a function of Reynolds numbers (10≤*Re*≤50) along with the micromixers; **(a)** M1, **(b)** M2, **(c)** M3, **(d)** M4 *(*v.l. represents the vertical length in millimeter which is the distance between the sections located on the y-axis and the origin of the microchannel)*

In Figure 12, the fluid streams are demonstrated at different locations of the M4 micromixer at *Re* = 20. Along with the first, second, and third sections, Dean flow does not become strong. Thus, minor transversal flow occurs, which can only lead to a slight deformation of the two streamlines. Water migrates from the outer wall of the microchannel, while Rhodamine B moves separately from the inner wall. Around the mid-spirals, the interface between the two fluid streams is deformed. As a result of the deformation, the water stream becomes narrower, while the Rhodamine B stream widens. As the fluids move to the outlet section, Rhodamine B contacts the outer wall for the first time in the sixth section of the M4 micromixer at *Re* = 20, and *M* becomes 0.63. At the end of the channel, the fluid streams mix into each other, and one unified stream can be observed, and a mixing index of 0.82 can be reached.

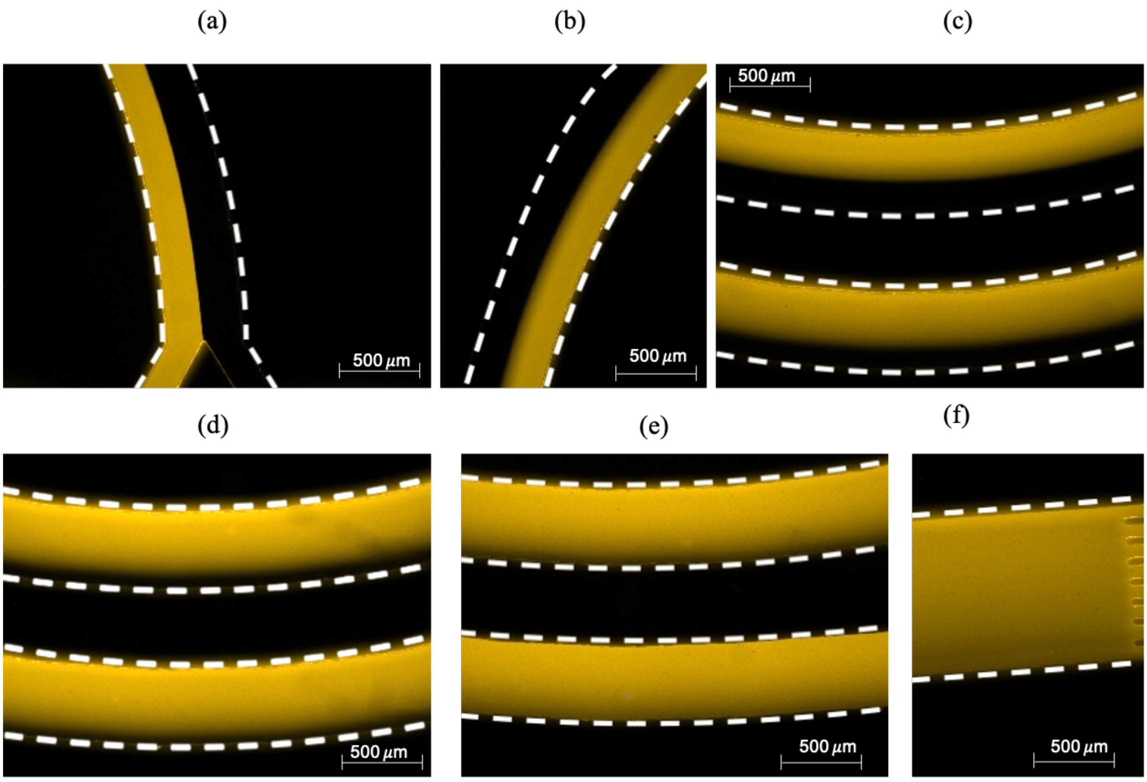

Figure 12. The fluorescence images of the development of mixing along with the flow direction in the M4 micromixer at *Re*=20. The black stream indicates water, the yellow stream indicates the diluted Rhodamine B solution, and the dark green stream depicts the mixed interface. Parallel yellow and black streams enter the M4 micromixer in the first section **(a)**. The following sections are denoted as **(b)** second, **(c)** third (upper) and fourth (lower), **(d)** fifth (upper) and sixth (lower), **(e)** seventh (upper) and eight (lower). Mixing is enhanced at the ninth section near the outlet of the M4 micromixers at *Re*=20, which is displayed with the dark green stream **(f)**.

As the Reynolds number increases from 20 to 30, the mixing indices more than 0.91 are achieved at the sections near the outlet for each micromixer at Re = 30 (Figure 11). The mixing index is 0.93 in the eight-section of the M1 micromixer, while it is 0.91, 0.93, and 0.92 in the ninth section of the M2, M3, and M4 micromixers, respectively. This is evident that the mixing performance is enhanced earlier at the sections near the outlet at low Reynolds numbers, ($Re \leq 30$). At $Re<50$, the maxima are observed in the last spirals of the micromixers. As a result, effective mixing can be achieved within all the mixers at $Re<50$.

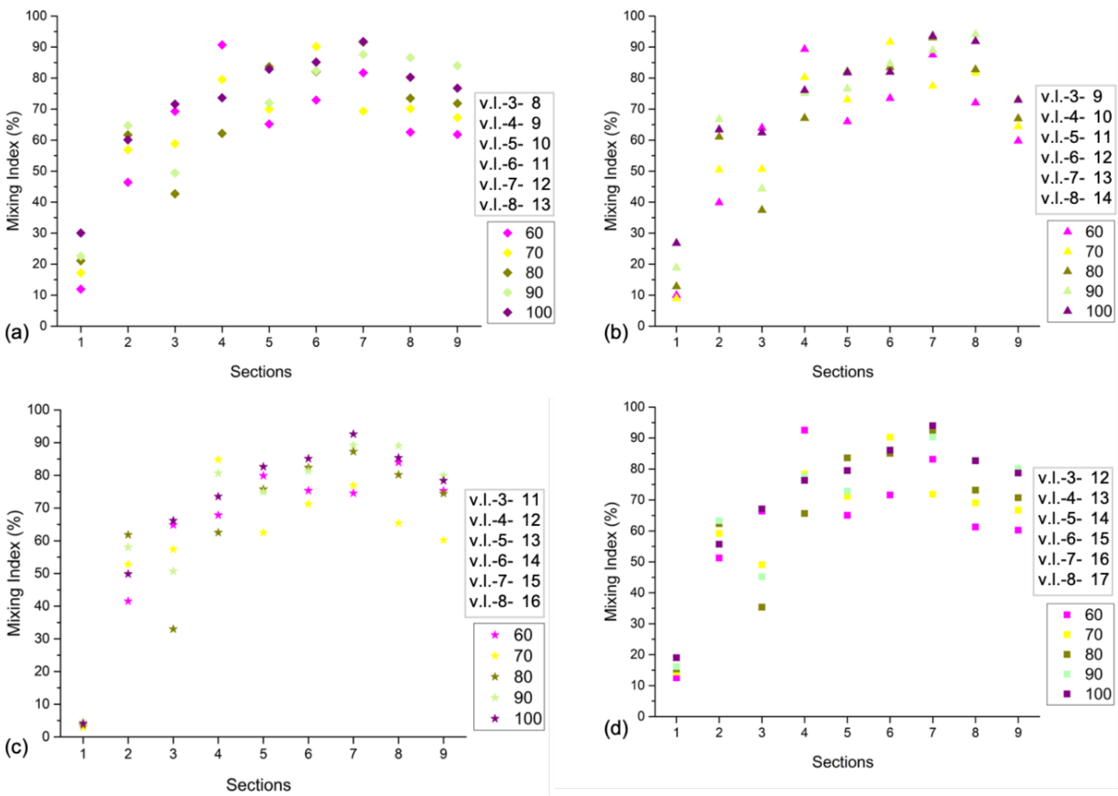

Figure 13. Mixing indexes as a function of Reynolds numbers (60≤*Re*≤100) along with the micromixers; **(a)** M1, **(b)** M2, **(c)** M3, **(d)** M4 *(*v.l. represents the vertical length in millimeter which is the distance between the sections located on the y-axis and the origin of the microchannel)*

At *Re* = 60, the local maxima shift to the fourth section for the M1, M2, and M4 micromixers, where the M values are 0.90, 0.89, and 0.92, respectively (Figure 13). The diffusion layer between the fluid streams is completely deformed in the third section and mixing is enhanced as 0.69, 0.64, 0.65, and 0.66 for M1, M2, M3, and M4 micromixers in their third sections, respectively. The local maximum in the fourth section occurs at *Re*= 70 for the M3 micromixer (as 0.85). The reason for the relatively low mixing performance of the M3 micromixer over most of the Reynolds number range is due to the varying radius along the microchannel. However, the M3 micromixer has the maximum mixing performance (M=0.96) at Re = 40 in the outlet section (Figure 11). As Reynolds increases from 60 to 70, the location, where the severe folding of the two-fluid streams occurs, shifted to the sixth section for the M1, M2, and M4 micromixers. Figure 14 represents the fluorescence images obtained from the third and fourth sections of each micromixer at *Re*= 70. In Figure 14, the breaking of the fluid streams starts to occur due to the stronger Dean flow in the third and the fourth sections, which causes an instant local decrease in the mixing efficiency. It should be noted that the main flow streams of the two fluids are replaced at these breaking points. For example, the mainstream of the water, which occurs at the outer wall of the microchannel at the third section, is replaced to the inner wall, which corresponded to the mainstream of the Rhodamine B. Moreover, the water stream near the inner wall at the third section moves towards the outer wall at the fourth section, and two fluid streams fold into each other because of the transversal motion along the spiral channel. This behavior of fluid streams leads to a more than 30% increase in the mixing index when moving from the third section to the fourth section. Thus, the mixing indices increase from 0.59, 0.51, 0.57, and 0.50 to 0.79, 0.80, 0.85, and 0.78 for the micromixers M1, M2, M3, and M4, respectively.

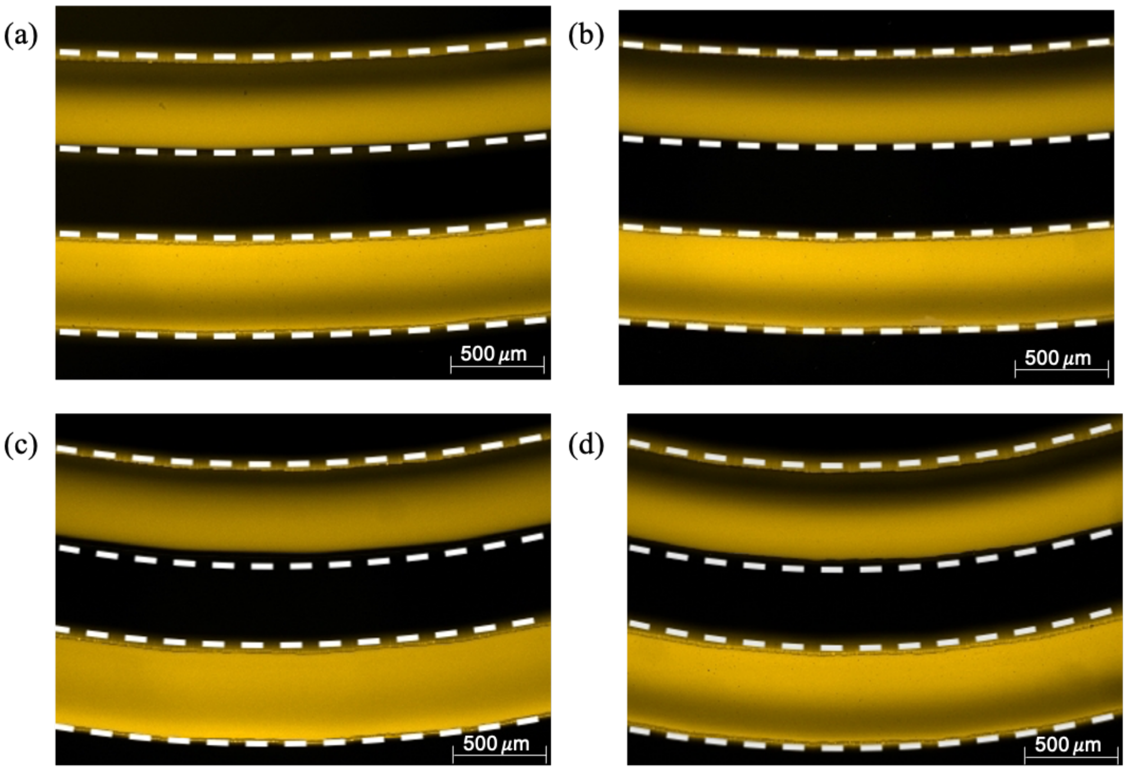

Figure 14. The fluorescence images of the progress of mixing at *Re*= 70 in the third and fourth sections of **(a)** M1, **(b)** M2, **(c)** M3, **(d)** M4 micromixers. The upper and lower microchannels depict the third and fourth sections, respectively. The water stream expands at the inner wall of the third section due to the strengthened Dean flow.

Figure 15 shows the fluid streamlines in the second section of the M3 micromixer at different Reynolds numbers and corresponding Dean numbers. The diffusion layer between the two fluid streams slightly deforms in at low Reynolds numbers Re<50 at the sections near the inlet, yet they flow along their main streamlines, where the water stream is located at the outer wall and the Rhodamine B stream is located at the inner wall of the channel (Figure 15a). An increase in the flow rate causes a proportional increase in the Dean number. Dean flow appears in the spiral microchannel and distorts the diffusion layer between the two-fluid streams at Re = 50 (with M as 0.29, Figure 15b). With the increase in flowrate, the Rhodamine B stream widens and completely covers the microchannel, which leads to an increase in the mixing index (M as 0.62) at Re = 80 in the second section (Figure 15c). A further increase in flowrate causes a decrease in the mixing performance (M=0.50 at Re = 100, Figure 15d), which is due to the exchange of locations of flow streams within the microchannel. The water stream is now located in the inner wall of the microchannel. Beyond Re = 100, the mixing performance improves in the second section by the presence of stronger Dean vortices, which repetitively stretch and provide twisting of the fluid streams.

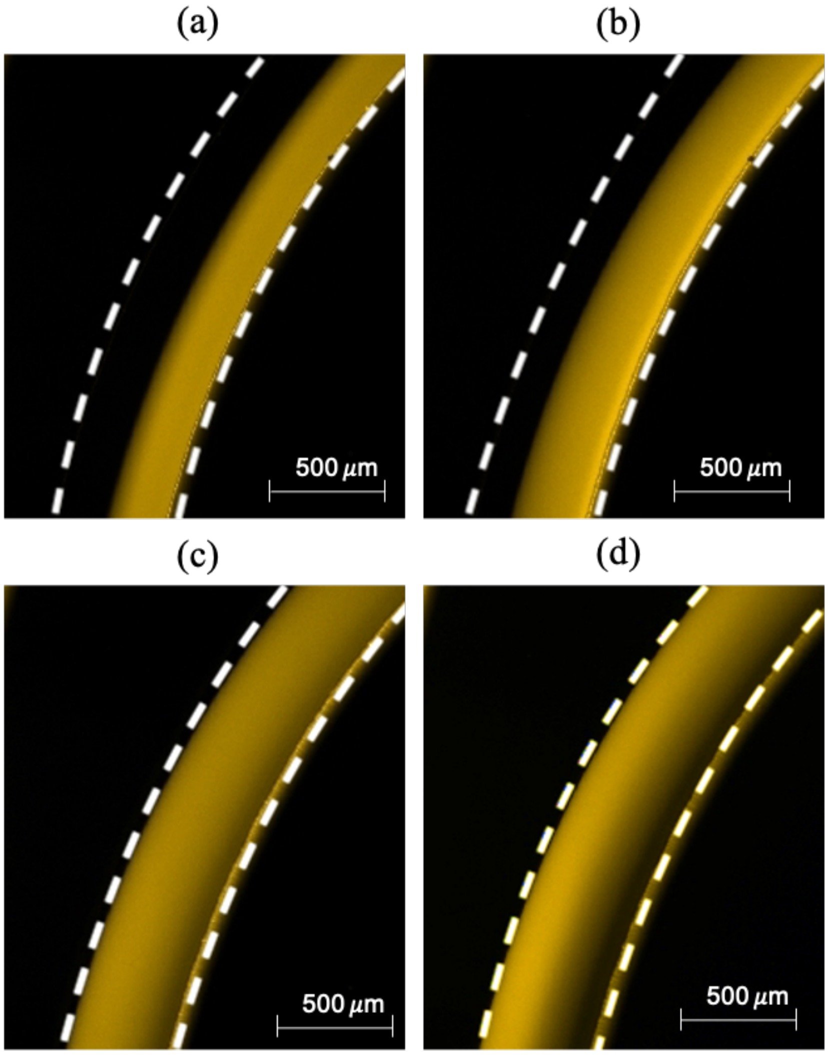

Figure 15. The fluorescence images, which are extracted from the second section of the M3 micromixer to evaluate the mixing progress at different Reynolds numbers and corresponding Dean numbers as **(a)** *Re*=20, *De*= 1.35 **(b)** *Re*=50, *De*= 3.38 **(c)** *Re*=80, *De*= 5.41 **(d)** *Re*=100, *De*= 6.76.

Over the Reynolds numbers range $80 \leq Re \leq 100$, the folding and stretching of the fluid streams at the last spirals (seventh and eighth sections) are apparent, which repetitively increases the mixing performance (Figure 13). The mentioned path lines of the two fluid streams show that fluid streams are located at different sections along the microchannel due to the variations in Dean numbers along the micromixers. Thus, it is hard to predict the exact locations of the breaking, stretching, and folding for the micromixers. The mixing indices in Figure 11 and Figure 13 clearly show that the dynamics and changes in locations related to the fluid streams cause a fluctuating trend in the mixing index along the micromixers beyond Reynolds numbers higher than 20.

Thus, the local maxima exist at different locations and Reynolds numbers for each micromixer. As an example, while higher mixing indices can be obtained at the spiral part of the micromixers M1, M2, and M4, the local maximum is located at the straight outlet (ninth section) for the M3 micromixer. When comparing the mixing indices at the spiral part of the micromixers, the local maxima occur at the eight sections of the micromixers M1 and M2 at Reynolds numbers 30 and 90 with *M* of 0.93 and 0.94, respectively, whereas the local maxima occur at the seventh section of the micromixers M3 and M4 at *Re*=100 with *M* of 0.93 and 0.94, respectively.

In short, it can be summarized that the breaking, stretching, and folding of the fluid streams can be observed locally at several locations along the micromixers at both relatively low ($Re \leq 50$) and high Reynolds numbers ($50 < Re \leq 100$). Thus, there exist certain maxima along the micromixers, where the mixing index *M* is more than 0.90 over the Reynolds numbers range, $10 \leq Re \leq 100$. Table 9 displays the vertical mixing length of the sections for each micromixer, where the maxima are located.

Table 9. The vertical mixing length of each micromixer which the maximum mixing efficiency are obtained for Reynolds numbers ($10 \leq Re \leq 100$) along the spiral part of the microchannels

Maximum mixing indices along the spiral part of the microchannels			
Mixer Types	Vertical Mixing Length (mm)	Mixing efficiency (%)	Reynolds numbers
M1	13	93	30
M2	14	94	90
M3	15	93	100
M4	16	94	100

The local maxima occur at the eight sections for the micromixers M1 and M2, while they form in the seventh section for the micromixers M3 and M4. When the initial aspect ratio of the microchannel decreases, the vertical mixing length corresponding to the local maxima increases.

3.1.3. The effect of expansion on mixing at the straight section of microchannels

The formation of expansion vortices is introduced to the flow by increasing the width of the straight channel (Rocha et al., 2007). The expansion causes a vortex flow at the entrance, which induces an upstream flow to the center. Sudarsan et. al. (Sudarsan & Ugaz, 2006) reported that the mixing performance could be increased at high flow rates by adding sudden expansions into the spiral microchannel designs. In this study, the width of the microchannel is gradually increased from 500 μm to 1000 μm at the straight part of the micromixer near the outlet section to observe the effect of expansion on the mixing performance in elliptic spiral micromixers.

Figure 16 displays the mixing index at the ninth (outlet) section for each micromixer. At *Re*= 10, the mixing index is smaller than 0.50 for each micromixer in the ninth section. Here, the diffusion layer between the two fluid streams is moderately manipulated. The Rhodamine B does not fully cover the microchannel due to the weak Dean flow along the microchannel. As *Re* increases from 10 to 20, the two fluid streams start to twist into each other, and the mixing index experiences a sudden increase at the ninth (outlet) section (from 0.44, 0.41, 0.44, and 0.48 to 0.62, 0.69, 0.69 and 0.82 for the M1, M2, M3, and M4 micromixers, respectively). A larger increase is observed at the outlet of the M4 micromixer at *Re* = 20, where *M* has a 70% jump from 0.48 to 0.82. The expansion at the outlet of the microchannel provides an increase in the mixing performance for all the mixers until *Re* = 30, where *M* becomes greater than 0.90 at their ninth section. A slight decrease is observed in the outlet *M* for the M1, M2, and M4 micromixers at *Re*= 40, while the maximum in the mixing index occurs at *Re* = 40 as 0.96 for the M3 micromixer, which reveals the remarkable effect of the expansion of the microchannel width so that the mixing index changes from 0.89 to 0.96 when moving from the eight-section to the straight outlet section.

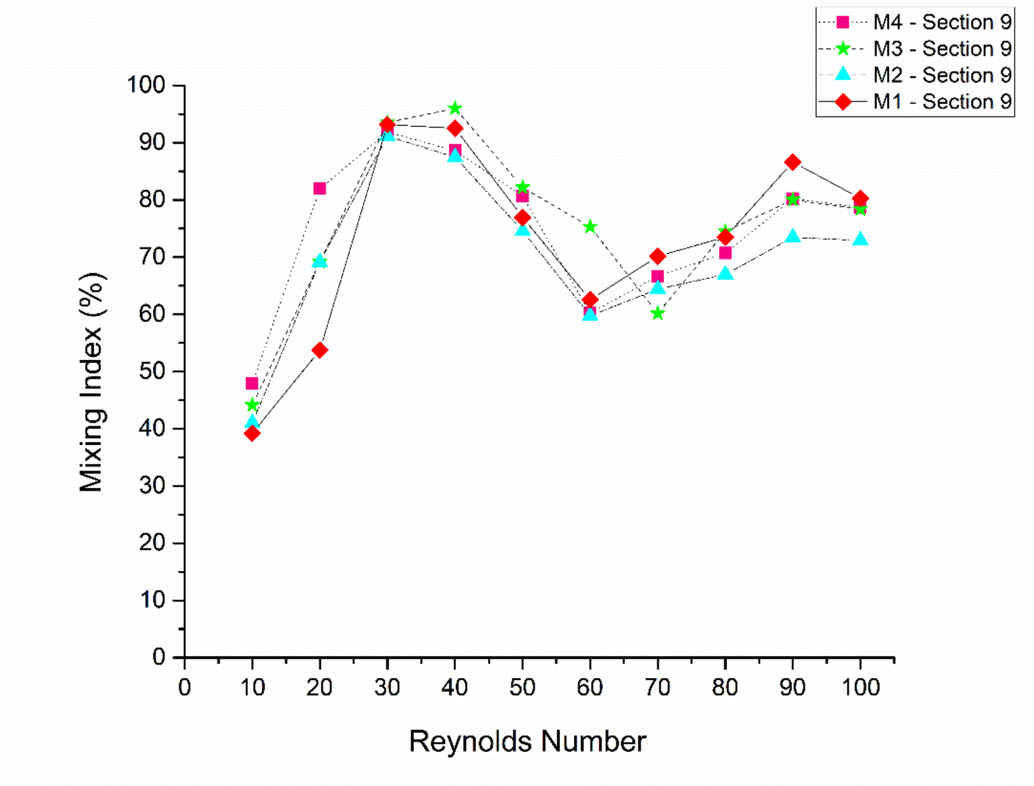

Figure 16. Mixing efficiency of four micromixers at ninth section corresponding to the straight part of the microchannel at the outlet.

The results indicate that mixing indices more than 0.90 can be achieved for all the micromixers at different locations, which suggests that the proposed micromixers are capable of providing perfect mixing at relatively small Reynolds numbers (≤100). The maximum mixing index as 0.96 is obtained at the outlet of the M3 micromixer at *Re* = 40, which is due to the reformative effect of the expansion of the channel width. Besides, the vertical mixing length is shortened for micromixers having higher initial aspect ratios.

3.2. Curved Micromixers with Various Baffle Geometries

3.2.1. The mixing performance analysis of the outlet M

Figure 17 displays the outlet mixing index (*M*) for all the micromixers (M1 to M7) for Reynolds and Dean numbers ranging from 1 to 50 and 0.39 to 19.36, respectively. Despite the availability of these two dimensionless numbers, for the sake of fair comparison with other types of micromixers in the literature, the results are explained only based on the Reynolds number.

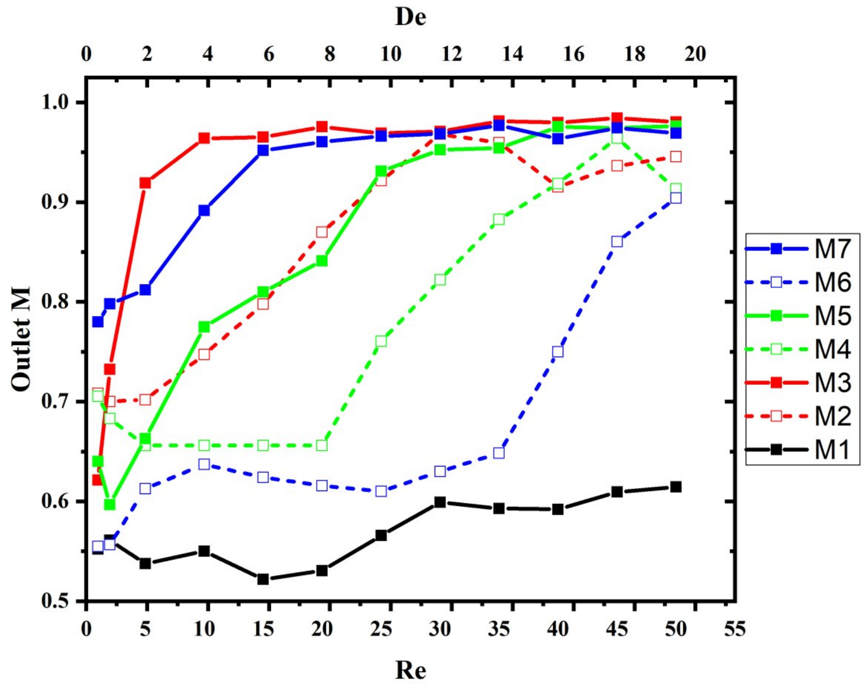

Figure 17. The values of outlet *M* against Re and De numbers for micromixers (M1 to M7)

Figure 17 shows that M1 has the lowest efficiency among the designed micromixers as expected, while M3 is the most efficient one. In addition to M3, the micromixers M5 and M7 exhibit a good mixing performance for high *Re*, which can be attributed to the higher number of designed baffles in the mentioned micromixers and consequently enhanced chaotic advection. The micromixers M2, M4, and M6 have lower mixing index values compared to their similar counterparts (i.e., M3, M5, and M7) but with more vortex generators (i.e., baffles). Also, it is observed that by increasing the fluid velocity, the generation of vortices by baffles increases (Santana et al., 2019) which consequently increases the mixing performance.

The outlet mixing index of the micromixer M1 is 0.55 at *Re*=1 and remains constant only with slight fluctuations until *Re*=15. Then, the mixing efficiency grows with the flow rate. Outlet *M* experiences its largest growth for this micromixer from 0.52 at *Re*=15 up to 0.60 at *Re*=30. It can be claimed that the induced secondary flow of curved microchannels improves the mixing quality since it generates partially chaotic advection (Xie & Xu, 2017). For *Re*≥30, outlet *M* approximately remains unchanged until *Re*=50, where the outlet mixing index is equal to 0.61 for M1 micromixer. The poor mixing performance indicates that the chaotic advection (Xie & Xu, 2017) is not initiated for M1 at the tested flow rates and Dean vortices only could moderately raise outlet M through the partially chaotic advection. Figure 18 shows the fluorescence intensity maps of M1 at *Re*=1, 25, and 50. It can be inferred that the secondary flows are not sufficiently strong to expand the diffusion layer, which is located at the interface of water and diluted Rhodamine B. That is the reason why it never covers the entire width of the micromixer despite partially widening of the diluted Rhodamine B stream width with the increase in fluid velocity.

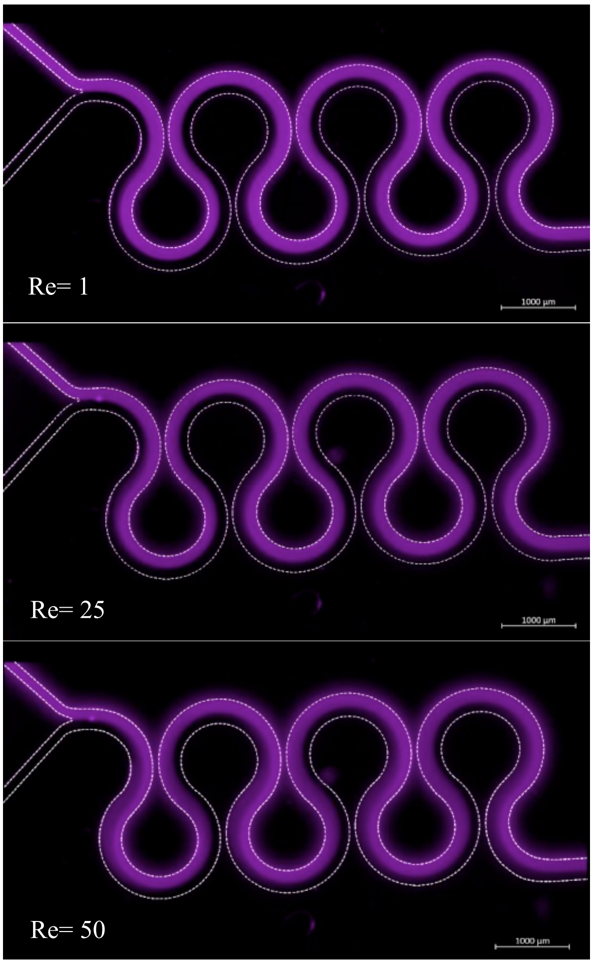

Figure 18. The fluorescence intensity maps of micromixer M1 at (a) *Re* = 1, (b) *Re* = 25, (c) *Re* = 50

Although the micromixer M2 has the outlet mixing index around 0.70 for $Re \leq 5$, it exhibits a rise beyond $Re > 1$ and reaches its highest efficiency with outlet *M* of 0.97 at *Re*=30. Vortex generation is dependent on the fluid velocity (Santana et al., 2019). Therefore, as *Re* approaches 30, the generated vortices and subsequent chaotic advection intensify and considerably enhance the mixing performance. Also, secondary vortices start to contribute to the mixing index enhancement and generate partially chaotic advection. For $30 \leq Re \leq 50$, there is a slight fluctuation, and outlet *M* is higher than 0.92. Figure 19a displays that the diffusion layer is eliminated for $Re \geq 25$.

The micromixer M3, which has the outlet *M* of 0.62 at *Re*= 1, experiences the sharpest increase among the designed micromixers and provides its best performance with a 0.98 mixing index at *Re*= 20. The initial relatively higher *M* values are present since the flow requires a longer time for low *Re* to arrive at the channel outlet and the species have more time to diffuse into each other (Bazaz et al., 2018; Santana et al., 2019). With the increase in the stream velocity, the partially chaotic and chaotic advection start to dominate the molecular diffusion. As an important result, this micromixer is capable of offering the highest mixing efficiency starting from a rather low *Re* (*Re*=20) compared to the other micromixers. Thus, the existence of more quasi-rectangular baffles in M3 compared to M2 (eight baffles compared to five in each arc) promotes the vortex generation for lower *Re*, which leads to the improvement in the mixing performance. Furthermore, the baffles can agitate the flow, which further enhances the mass transfer rate (Bazaz et al., 2018). Beyond *Re*=20, the mixing efficiency remains stable only with negligible changes between 0.98 and 0.97 implying that even low fluid velocities are sufficient for this type of micromixer to provide excellent mixing. The explained trend for M3 can be also observed in the fluorescence intensity maps displayed in Figure 19b.

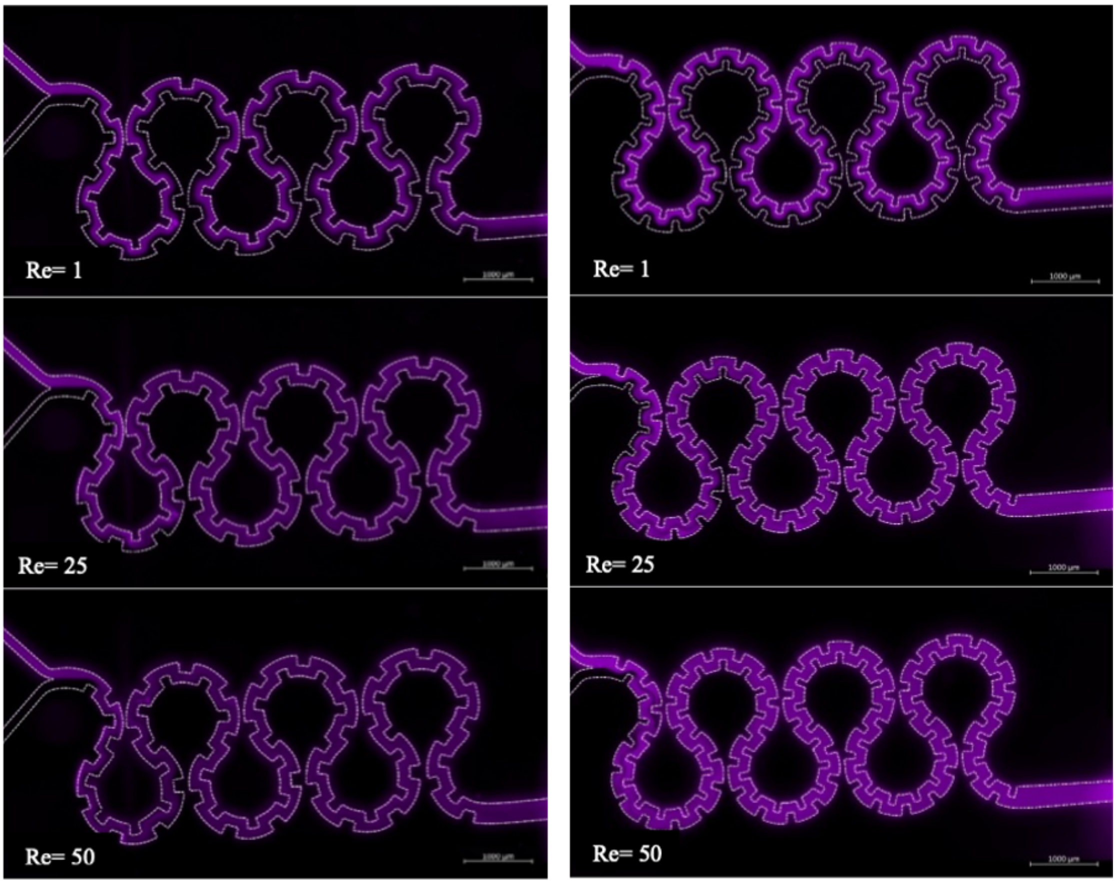

(a) (b)

Figure 19. The fluorescence intensity maps of micromixer (a) M2 and (b) M3 at *Re* = 1, 25, and 50

The outlet *M* of the micromixer M4 slightly decreases from 0.71 to 0.66 as *Re* increases from 1 to 5 and then maintains at the same level until *Re*= 20. The relatively higher mixing efficiency at the initial flow rates can be explained by the fact that molecular diffusion is the dominant mass transfer mechanism. In other words, the species have a longer time to move to the opposite side of the channel or to deform the diffusion layer. While there is a plateau for $5 \leq Re \leq 20$, with the intensified Dean vortices and the resulting chaotic advection, the outlet *M* significantly increases to 0.96, when *Re* is raised from 20 to 45. The reason for the minor widening of the diluted Rhodamine B flow stream in *Re* lower than 25 (Figure 20a) is the presence of weak Dean vortices.

The micromixer M5, similar to its counterpart (i.e., M4), initially shows a higher outlet *M* value of 0.64 at *Re*= 1 and then slowly decreases to 0.60 when *Re* is 2. It can be inferred that for M4 and M5 with forward-triangular baffle configuration, the molecular diffusion mainly contributes to enhancing the mixing efficiency at the beginning. Also, the following decrease can be attributed to the reduced diffusion time because of the fluid velocity increase (Santana et al., 2019). Subsequently, the outlet *M* increases from 0.60 to 0.98 within the range of $2 \leq Re \leq 40$. Here, with the initiation of the secondary flows effect and chaotic advection, especially for relatively higher *Re* (i.e., $Re \geq 15$), an increase beyond the decreasing region is apparent. The outlet *M* remains almost unchanged beyond *Re*=40, which suggests perfect mixing (Figure 20b).

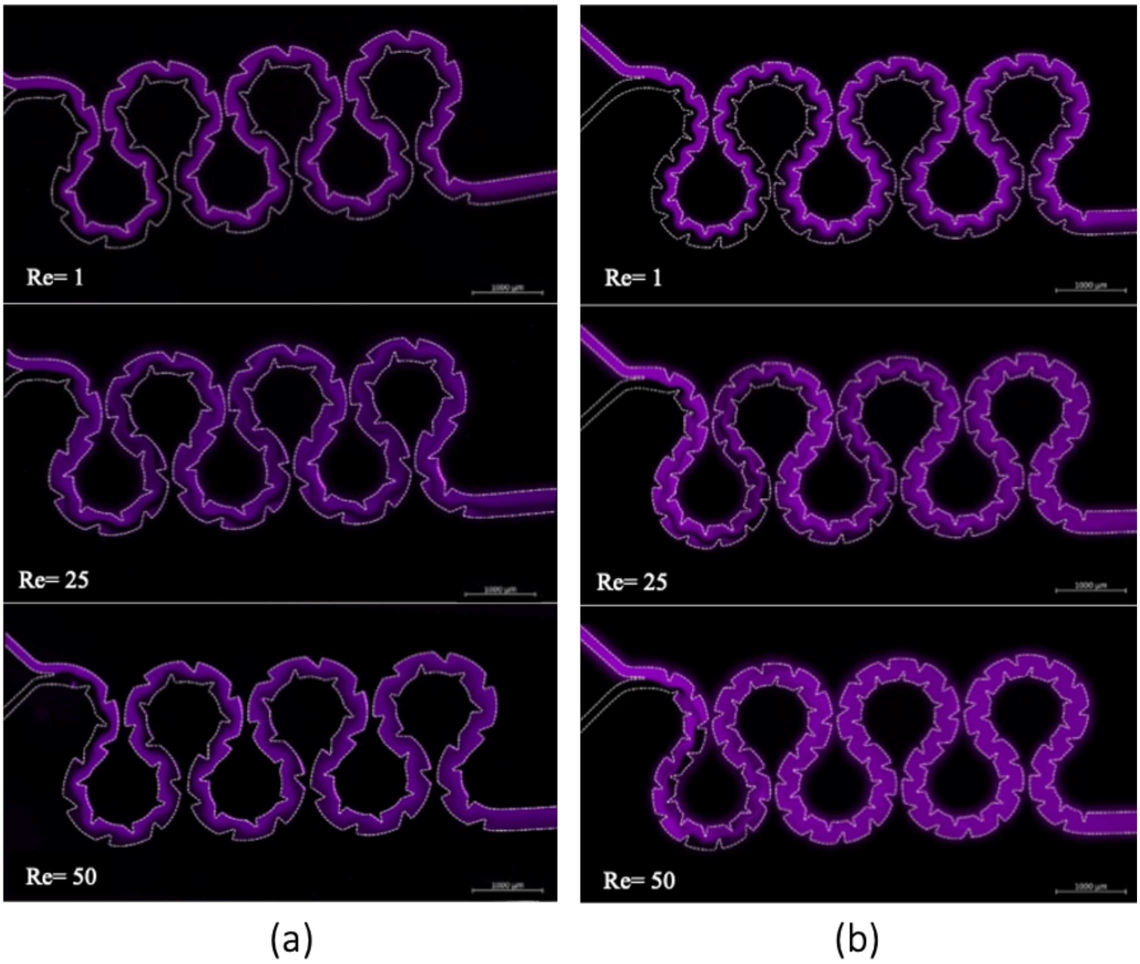

Figure 20. The fluorescence intensity maps of micromixer (a) M4 and (b) M5 at *Re* = 1, 25, and 50

The micromixer M6 has the lowest mixing performance for the studied flow rates, when M1, the base of comparison, is excluded. The outlet *M* value of M6 starts from 0.55 and grows to 0.64 when *Re* is 10. Most probably, for this micromixer, the molecular diffusion is dominant for Reynolds numbers lower than the smallest Reynolds number value in this study, and its effect decreases with the flow velocity at a low range of *Re* (Santana et al., 2019). The outlet mixing index remains almost unchanged with a small fluctuation until *Re* of 35. It can be deduced that the partially chaotic advection (Xie & Xu, 2017) is not noticeably influential for the mentioned range. Subsequently, owing to the chaotic advection impact, there is an upward trend up to the end of the experiment (*Re*=50) where *M*= 0.90. There is a similar trend between M6 and M4; however, the delay in chaotic advection affects the mixing efficiency of M6. Figure 21a proves that the diffusion layer remains until the highest flow rate (*Re*=50), and only minor widening occurs for lower fluid velocities.

The micromixer M7 has the best performance among the designed micromixers for the lowest flow rates (i.e., *Re*= 1 and 2) with the corresponding outlet *M* values of 0.78 and 0.80, respectively. For 1≤ *Re* ≤ 35, outlet M experiences an upward trend (from 0.78 to 0.98). Interestingly, the lowest mixing index of 0.78 at *Re*=1 is related to the vortex generation at a wide range of *Re* and consequently enhanced mixing performance. When comparing M6 to M7 both with backward triangular baffles, it can be concluded that the number of baffles is an important parameter since the baffles accelerate chaotic advection through the constantly folding and stretching of the fluid. Eventually, for *Re* ≥ 35, there is not any significant change. Accordingly, at *Re* = 25, where *M*=0.97, the diluted Rhodamine B stream uniformly covers the channel outlet region as shown in Figure 21b.

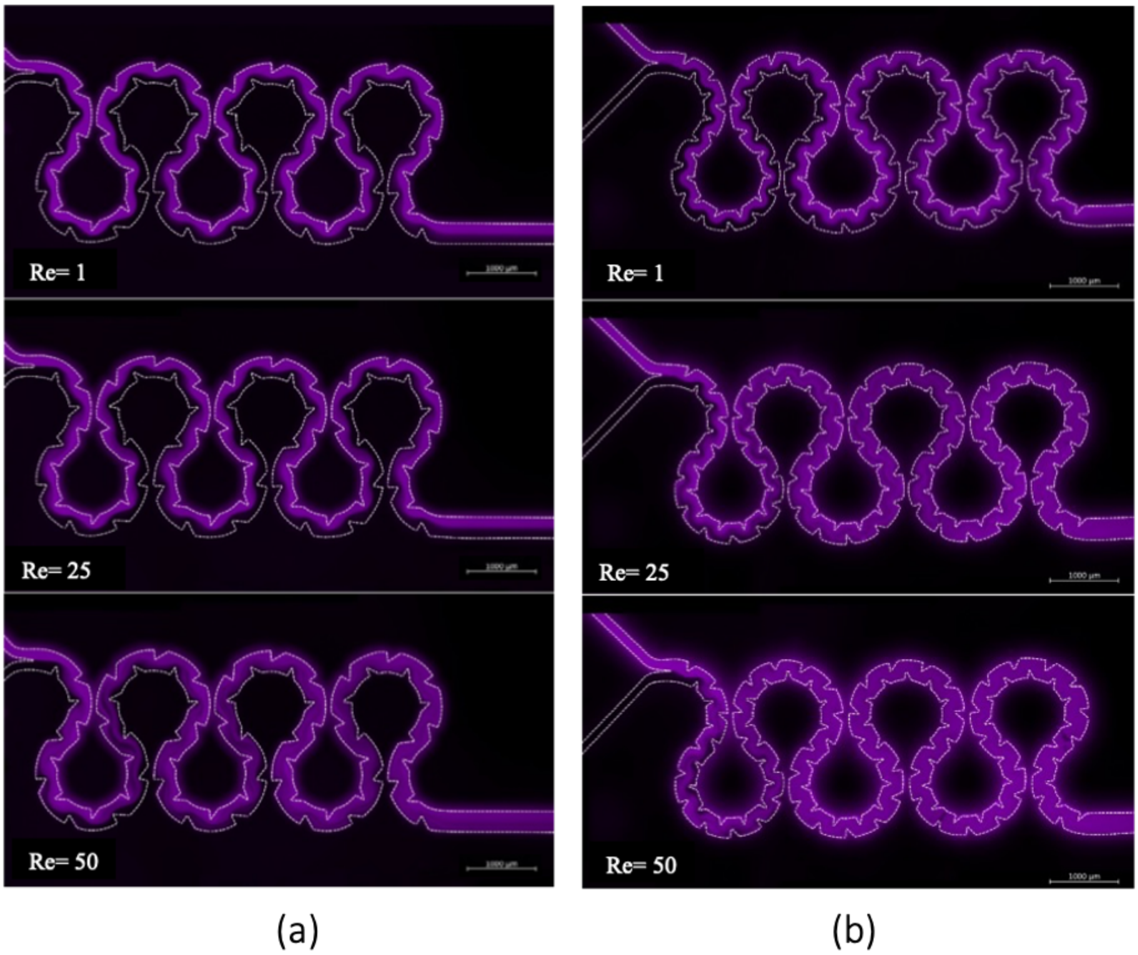

Figure 21. The fluorescence intensity maps of micromixer (a) M6 and (b) M7 at *Re* = 1, 25, and 50

Overall, the designed baffles continuously decrease the stream width over the channel, which results in enlarged contact between the fluids and enhanced mixing (Santana et al., 2019). The generated secondary flow in serpentine micromixers intensifies with an increase in *Re*. Also, vortex generation by designed baffles and chaotic advection depend on the fluid velocity. The effect of baffle number is obvious for all similar cases, particularly for M6 and M7.

3.2.2. Investigation of mixing efficiency along the micromixers

Figure 22 presents the mixing behavior along the micromixers by supplying *M* values at four different locations along their longitudinal length, which is 22.64 mm. The measured locations (i.e., 3.38, 9.73, 16.08, and 22.64 mm) correspond to the first, third, and fifth segments as well as the channel outlet (as marked by green lines in Figure 2).

In Figure 22a, M7 provides the best mixing performance at the measured locations except the first one. Even though M3 and M5 are one of the best mixers, their corresponding mixing indices at *Re*=1 until the fifth segment are even lower than M1. It can be concluded that while the chaotic advection for M7 is effective even in the first segment, it lately contributes to intermix the fluids within M3 and M5. This proves that backward baffles are capable to generate a larger number of vortices at smaller fluid velocities highlighting the impact of baffle designs. Among the micromixers, the largest increase occurs for M5 at the first transition with 95%, where M changes from 0.20 to 0.39. However, there is only 2% growth at the last transition for M6, and the *M* value changes from 0.54 to 0.55.

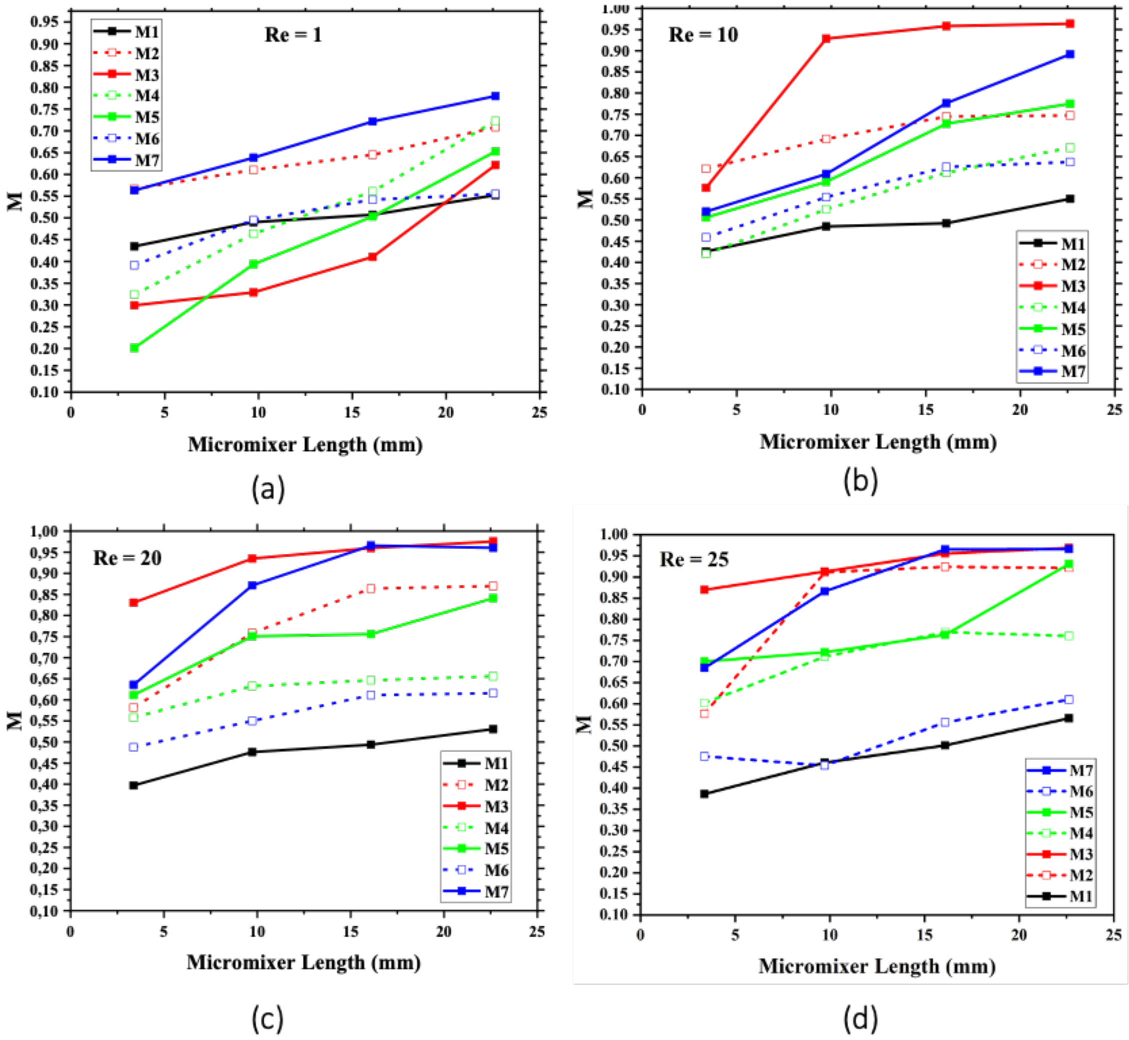

Figure 22. Variation of *M* along the micromixers for *Re* of **(a)** 1, **(b)** 10, **(c)** 20, **(d)** 25

Figure 22b shows that the mixing index of M3 experiences a 61% jump from 0.58 to 0.93 at the first transition, while there is no considerable increase afterward. Although there is not effective mixing in the first segment, the diffusion layer is completely gone in the third segment. The mixing efficiency of M7 is continuously improved along the channel, and the biggest rise happens with 27% at the second transition where the diluted Rhodamine B solution approaches to water side wall moving along the channels. The mixing capability of M2 remains stable without any change when the fluid flows from the fifth segment toward the outlet.

The mixing index of M7 increases by 37%, from 0.64 to 0.87, at the first transition as the largest rise for *Re*=20, shown in Figure 22c. Comparing the M values along the microchannel in Figure 22a, Figure 22b, and Figure 22c, the generated chaotic advection with the increase in fluid velocity contributes to the initial segments and improves the mixing efficiency. The smallest change from the first measured location to the outlet happens for M3 micromixer which has quasi-rectangular baffles, where M increases by 17%, from 0.83 to 0.98, implying that the geometry of these micromixers is capable to provide higher mixing qualities even at the lower longitudinal lengths.

It is also seen in Figure 22d that the M3 micromixer (from the first measurement location) has the best mixing performance compared to others. It can be inferred that the quasi-rectangular baffles properly contribute to the stretching and folding of the fluid. Among the presented cases at $Re = 25$, the mixing index of M2 at the first transition (from the first to the third segment) possesses the largest increase with 58%, from 0.58 to 0.91.

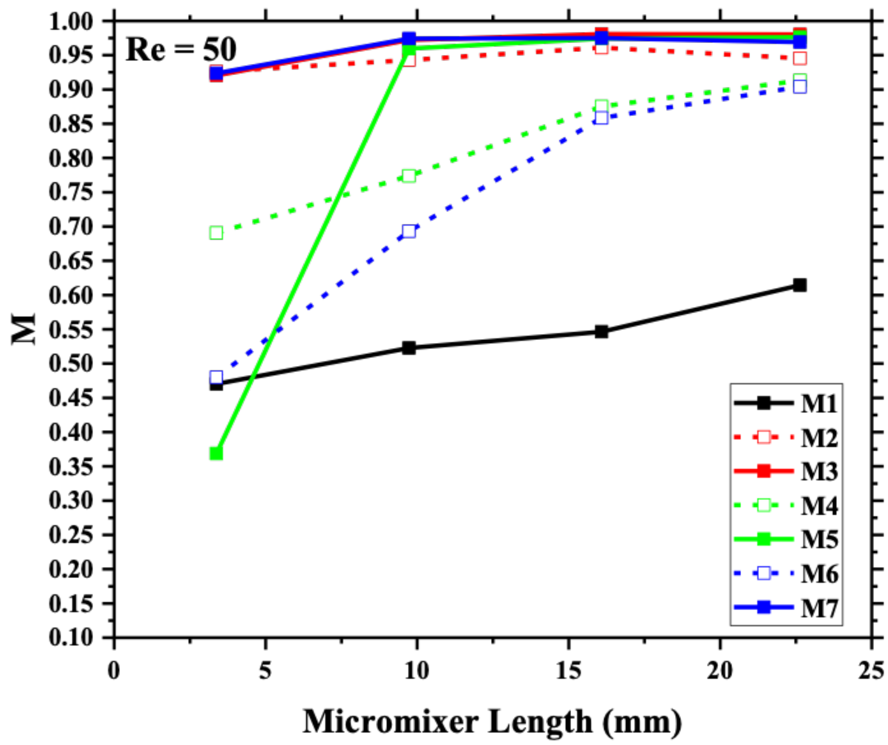

Figure 23. Variation of M along the micromixers for Re= 50

Figure 23 represents the mixing indices variation along the micromixers at Re = 50. The M value for M5 suddenly increases by 160% from 0.37 to 0.96 when moving from the first to the second measured location, which corresponds to the biggest rise compared to the previous location among the presented micromixers. This phenomenon can be explained noticing Figure 20b (Re=50), where the low-intensity regions in the first segment are eliminated in this case through the first transition resulting in a sudden jump of *M* value. Besides, M2 experiences the smallest change at *Re*=50 and the M value decreases by 2% at the last transition, which is the largest decrease among the presented cases of Figure 22 and Figure 23. Overall, as the fluid moves from the inlet to the outlet, *M* values experience an increasing trend implying that chaotic advection increases from inlet to outlet.

CHAPTER 4.

CONCLUSION AND FUTURE WORK

4.1. Concluding Remarks of Spiral Elliptic Micromixers

In this study, the elliptic micromixers having five-loop spiral designs with different initial aspect ratios were presented. The optimum Reynolds numbers corresponding to the local maxima of mixing are identified for each micromixer. Mixing indices up to 0.91 is obtained at the sections near the outlet for each micromixer at *Re* =30 which makes the elliptical spiral microchannels a preferable option comparing the other passive micromixers. Mixing indices more than 0.90 are observed at Reynolds numbers ranging from 10 to 100 at mid-spirals and last spirals. The locations of local maxima differ for each microchannel due to the effect of the varying curvature radius. At a relatively low Reynolds number ($Re \leq 50$), the maximum mixing performance of 0.96 is observed in the micromixer M3 at *Re* = 40 because of the presence of expansion at the straight outlet section, whereas the maxima are located at spiral parts for the micromixers M1, M2, and M4. Accordingly, the M1 micromixer leads to a mixing index of 0.93 at *Re* = 30. The micromixers M2 and M4 have the maximum mixing indices of 0.94 at *Re* = 90 and *Re* = 100, respectively. Comparing the mixing performance of the micromixers at their spiral parts, the locations of maxima are located at the eighth sections for the M1 and M2 micromixers and the seventh sections for the M3 and M4 micromixers. Due to the different initial aspect ratios of the microchannels, the vertical mixing length increases for the micromixers M3 and M4, which have relatively low initial aspect ratios.

The fabrication of the proposed design can be achieved by the single-step standard lithography process, which is a cost-effective method. Polydimethylsiloxane micromixers can easily be integrated into the various microfluidics platforms. The change in the mixing performance at different locations of the microchannel can be useful for several biological and chemical applications, which initially require the mixing of two compounds and their separation afterward. According to the desired application, the micromixer length could also be reduced by eliminating the number of loops.

4.2. Concluding Remarks of Curved Micromixers with Various Baffle Geometries

In this study, it was aimed to enhance the mixing performance by introducing baffles into the sidewalls of curved serpentine micromixers. The micromixer M1 with no baffles was the base of comparison. The designed baffle geometries were quasi-rectangular (M2, M3), forward triangular (M4, M5), and backward triangular (M6, M7), where only the number of baffles increased between the similar counterparts. These baffles generated vortices to enhance chaotic advection and consequently mixing index. According to the experimental results for $1 \leq Re \leq 50$, the maximum outlet M for the micromixer M1 at the tested flow rates was 0.61. Accordingly, Dean vortices could moderately raise the outlet M through partially chaotic advection. However, due to the existence of constant fluid folding and stretching in micromixers with baffles, the mixing index values could be significantly increased. The micromixer M3 provided the highest outlet mixing index (M) of 0.98 at Re=20, implying that chaotic advection could enhance the mixing efficiency even at low Re. Also, the same outlet M was obtained for the micromixers M5 and M7 at Re= 40 and 35, respectively. Even though the similar counterparts of these micromixers (i.e., M2, M4, and M6) could provide high outlet M, for instance, 0.97 at Re=30 for the micromixer M2, the chaotic advection contributed at rather higher fluid velocities. Overall, the micromixers M3 and M7 had the best mixing performances among others.

4.3. Future Work

Soon, the elliptical spiral microchannel designs will be utilized for the separation of circulating tumor cells (CTCs). Additionally, the focusing mechanism of the CTCs will be revealed by correlating the presented flow dynamics in the microchannel.

For both micromixer designs (elliptical spiral and curved serpentine microchannels with baffles), the effect of the aspect ratio and hydraulic diameter could be investigated for better mixing efficiencies. By changing the inner and outer radii of the serpentine micromixers, the mixing performance could be improved.

The wall of the elliptic spiral micromixers could be modified with the quasi-rectangular baffles, which performed the most efficient mixing for the serpentine micromixers, to increase the mixing performance further

All the designed micromixers will be integrated into lab-on-a-chip devices in near future for the diagnosis of diseases and synthesis of nanomaterials including graphene.

BIBLIOGRAPHY

Akgönül, S., Özbey, A., Karimzadehkhouei, M., Gozuacik, D., & Koşar, A. (2017). The effect of asymmetry on micromixing in curvilinear microchannels. *Microfluidics and Nanofluidics*, *21*(7), 1–15. https://doi.org/10.1007/s10404-017-1952-1

Al-Halhouli, A., Alshare, A., Mohsen, M., Matar, M., Dietzel, A., & Büttgenbach, S. (2015). Passive micromixers with interlocking semi-circle and omega-shaped modules: Experiments and simulations. *Micromachines*, *6*(7), 953–968. https://doi.org/10.3390/mi6070953

Alam, A., Afzal, A., & Kim, K.-Y. Y. (2014). Mixing performance of a planar micromixer with circular obstructions in a curved microchannel. *Chemical Engineering Research and Design*, *92*(3), 423–434. https://doi.org/10.1016/j.cherd.2013.09.008

Alam, A., & Kim, K. Y. (2012). Analysis of mixing in a curved microchannel with rectangular grooves. *Chemical Engineering Journal*, *181–182*, 708–716. https://doi.org/10.1016/j.cej.2011.12.076

Alijani, H., Özbey, A., Karimzadehkhouei, M., & Koşar, A. (2019). Inertial micromixing in curved serpentine micromixers with different curve angles. *Fluids*, *4*(4), 1–17. https://doi.org/10.3390/fluids4040204

Ansari, M. A., Kim, K.-Y. Y., Anwar, K., & Kim, S. M. (2010). A novel passive micromixer based on unbalanced splits and collisions of fluid streams. *Journal of Micromechanics and Microengineering*, *20*(5), 055007. https://doi.org/10.1088/0960-1317/20/5/055007

Baheri Islami, S., Khezerloo, M., & Gharraei, R. (2017). The effect of chaotic advection on mixing degree and pressure drop of non-Newtonian fluids flow in curved micromixers. *Journal of the Brazilian Society of Mechanical Sciences and Engineering*, *39*(3), 813–831. https://doi.org/10.1007/s40430-016-0689-1

Bayareh, M., Ashani, M. N., & Usefian, A. (2020). Active and passive micromixers: A comprehensive review. *Chemical Engineering and Processing - Process Intensification*, *147*(November 2019), 107771. https://doi.org/10.1016/j.cep.2019.107771

Bazaz, S. R., Mehrizi, A. A., Ghorbani, S., Vasilescu, S., Asadnia, M., & Warkiani, M. E. (2018). A hybrid micromixer with planar mixing units. *RSC Advances*, *8*(58), 33103–33120.

Bhagat, A. A. S., Kuntaegowdanahalli, S. S., & Papautsky, I. (2008). Continuous particle separation in spiral microchannels using dean flows and differential migration. *Lab on a Chip*, *8*(11), 1906–1914. https://doi.org/10.1039/b807107a

Bhagat, A. A. S., & Papautsky, I. (2008). Enhancing particle dispersion in a passive planar micromixer using rectangular obstacles. *Journal of Micromechanics and Microengineering*, *18*(8). https://doi.org/10.1088/0960-1317/18/8/085005

Bhagat, A. A. S., Peterson, E. T. K., & Papautsky, I. (2007). A passive planar micromixer with obstructions for mixing at low Reynolds numbers. *Journal of Micromechanics and Microengineering*, *17*(5), 1017–1024. https://doi.org/10.1088/0960-1317/17/5/023

Bilsel, O., Kayatekin, C., Wallace, L. A., & Matthews, C. R. (2005). A microchannel solution mixer for studying microsecond protein folding reactions. *Review of Scientific Instruments*, *76*(1), 014302. https://doi.org/10.1063/1.1834698

Cai, G., Xue, L., Zhang, H., & Lin, J. (2017). A review on micromixers. *Micromachines*, *8*(9). https://doi.org/10.3390/mi8090274

Chen, J. J., Chen, C. H., & Shie, S. R. (2011). Optimal designs of staggered dean vortex micromixers. *International Journal of Molecular Sciences*, *12*(6), 3500–3524. https://doi.org/10.3390/ijms12063500

Dean, W. R., & Hurst, J. M. (1959). Note the motion of fluid in a curved pipe. *Mathematika*, *6*(1), 77–85. https://doi.org/10.1112/S0025579300001947

Di Carlo, D. (2009). Inertial microfluidics. *Lab on a Chip*, *9*(21), 3038–3046. https://doi.org/10.1039/b912547g

Duryodhan, V. S., Chatterjee, R., Govind Singh, S., & Agrawal, A. (2017). Mixing in planar spiral microchannel. *Experimental Thermal and Fluid Science*, *89*(July), 119–127. https://doi.org/10.1016/j.expthermflusci.2017.07.024

Erdem, K., Ahmadi, V. E., Kosar, A., & Kuddusi, L. (2020). Differential sorting of microparticles using spiral microchannels with elliptic configurations. *Micromachines*, *11*(4). https://doi.org/10.3390/MI11040412

Gambhire, S., Patel, N., Gambhire, G., & Kale, S. (2011). A Review on Different Micromixers and its Micromixing within Microchannel. *International Journal of Current Engineering and Technology*, *March*. https://doi.org/10.14741/ijcet/22774106/spl.4.2016.83

Gobby, D., Angeli, P., & Gavriilidis, A. (2001). Mixing characteristics of T-type microfluidic mixers. *Journal of Micromechanics and Microengineering*, *11*(2), 126–132. https://doi.org/10.1088/0960-1317/11/2/307

Guzniczak, E., Otto, O., Whyte, G., Willoughby, N., Jimenez, M., & Bridle, H. (2020). Deformability-induced lift force in spiral microchannels for cell separation. *Lab on* *a Chip*, *20*(3), 614–625. https://doi.org/10.1039/c9lc01000a

Hao, N., Xu, Z., Nie, Y., Jin, C., Closson, A. B., Zhang, M., & Zhang, J. X. J. (2019). Microfluidics-enabled rational design of ZnO micro-/nanoparticles with enhanced photocatalysis, cytotoxicity, and piezoelectric properties. *Chemical Engineering Journal*, *378*(April), 122222. https://doi.org/10.1016/j.cej.2019.122222

Hessel, V., Hofmann, C., Löb, P., Löhndorf, J., Löwe, H., & Ziogas, A. (2005). Aqueous Kolbe-Schmitt synthesis using resorcinol in a microreactor laboratory rig under high-p,T conditions. *Organic Process Research and Development*, *9*(4), 479–489. https://doi.org/10.1021/op050045q

Hong, C. C., Choi, J. W., & Ahn, C. H. (2004). A novel in-plane passive microfluidic mixer with modified Tesla structures. *Lab on a Chip*, *4*(2), 109–113. https://doi.org/10.1039/b305892a

Iwasaki, T., & Yoshida, J. I. (2005). Free radical polymerization in microreactors. Significant improvement in molecular weight distribution control. *Macromolecules*, *38*(4), 1159–1163. https://doi.org/10.1021/ma048369m

Jeon, H., Massoudi, M., & Kim, J. (2017). Magneto-hydrodynamics-driven mixing of a reagent and a phosphate-buffered solution: A computational study. *Applied Mathematics and Computation*, *298*, 261–271. https://doi.org/10.1016/j.amc.2016.11.026

Jeong, G. S., Chung, S., Kim, C. B., & Lee, S. H. (2010). Applications of micromixing technology. *Analyst*, *135*(3), 460–473. https://doi.org/10.1039/b921430e

Karnik, R. (2008). Microfluidic Mixing. *Encyclopedia of Microfluidics and Nanofluidics*, *2*, 1177–1186. https://doi.org/10.1007/978-0-387-48998-8_939

Kim, S. J., Wang, F., Burns, M. A., & Kurabayashi, K. (2009). Temperature-programmed natural convection for micromixing and biochemical reaction in a single microfluidic chamber. *Analytical Chemistry*, *81*(11), 4510–4516. https://doi.org/10.1021/ac900512x

Li, J., Xia, G., & Li, Y. (2013). Numerical and experimental analyses of planar asymmetric split-and-recombine micromixer with dislocation sub-channels. *Journal of Chemical Technology and Biotechnology*, *88*(9), 1757–1765. https://doi.org/10.1002/jctb.4044

Li, Z., & Kim, S. J. (2017). Pulsatile micromixing using water-head-driven microfluidic oscillators. *Chemical Engineering Journal*, *313*, 1364–1369. https://doi.org/10.1016/j.cej.2016.11.056

Lim, E., Lee, L., Yeo, L. Y., Hung, Y. M., & Tan, M. K. (2019). Acoustically driven micromixing: Effect of transducer geometry. *IEEE Transactions on Ultrasonics, Ferroelectrics, and Frequency Control*, *66*(8), 1387–1394. https://doi.org/10.1109/TUFFC.2019.2920683

Mae, K., Maki, T., Hasegawa, I., Eto, U., Mizutani, Y., & Honda, N. (2004).

Development of a new micromixer based on split/recombination for mass production and its application to soap free emulsifier. *Chemical Engineering Journal*, *101*(1–3), 31–38. https://doi.org/10.1016/j.cej.2003.10.011

Mashaei, P. R., Asiaei, S., & Hosseinalipour, S. M. (2020). Mixing efficiency enhancement by a modified curved micromixer: A numerical study. *Chemical Engineering and Processing - Process Intensification*, *154*(July). https://doi.org/10.1016/j.cep.2020.108006

Mehrdel, P., Karimi, S., Farré-Lladós, J., & Casals-Terré, J. (2018). Novel variable radius spiral-shaped micromixer: From numerical analysis to experimental validation. *Micromachines*, *9*(11). https://doi.org/10.3390/mi9110552

Meng, J., Li, S., Li, J., Yu, C., Wei, C., & Dai, S. (2018). AC electrothermal mixing for high conductive biofluids by arc-electrodes. *Journal of Micromechanics and Microengineering*, *28*(6). https://doi.org/10.1088/1361-6439/aab39b

Microchem. (2000). SU-8 3000 Permanent Epoxy Negative Photoresist. *Product Datasheet*, *20*.

Nagaki, A., Kawamura, K., Suga, S., Ando, T., Sawamoto, M., & Yoshida, J. I. (2004). Cation pool-initiated controlled/living polymerization using microsystems. *Journal of the American Chemical Society*, *126*(45), 14702–14703. https://doi.org/10.1021/ja044879k

Nie, Y., Hao, N., & Zhang, J. X. J. (2017). Ultrafast Synthesis of Multifunctional Submicrometer Hollow Silica Spheres in Microfluidic Spiral Channels. *Scientific Reports*, *7*(1), 1–9. https://doi.org/10.1038/s41598-017-12856-9

Nivedita, N., Ligrani, P., & Papautsky, I. (2017). Dean Flow Dynamics in Low-Aspect Ratio Spiral Microchannels. *Scientific Reports*, *7*(October 2016), 1–10. https://doi.org/10.1038/srep44072

Orbay, S., Ozcelik, A., Lata, J., Kaynak, M., Wu, M., & Huang, T. J. (2017). Mixing high-viscosity fluids via acoustically driven bubbles. *Journal of Micromechanics and Microengineering*, *27*(1), 015008. https://doi.org/10.1088/0960-1317/27/1/015008

Park, T., Lee, S., Seong, G. H., Choo, J., Lee, E. K., Kim, Y. S., Ji, W. H., Hwang, S. Y., Gweon, D. G., & Lee, S. (2005). Highly sensitive signal detection of duplex dye-labelled DNA oligonucleotides in a PDMS microfluidic chip: Confocal surface-enhanced Raman spectroscopic study. *Lab on a Chip*, *5*(4), 437–442. https://doi.org/10.1039/b414457k

Rahman Nezhad, J., & Mirbozorgi, S. A. (2018). An immersed boundary-lattice Boltzmann method to simulate chaotic micromixers with baffles. *Computers and Fluids*, *167*, 206–214. https://doi.org/10.1016/j.compfluid.2018.02.031

Rani, S. A., Pitts, B., & Stewart, P. S. (2005). Rapid diffusion of fluorescent tracers into Staphylococcus epidermidis biofilms visualized by time lapse microscopy.

Antimicrobial Agents and Chemotherapy, *49*(2), 728–732. https://doi.org/10.1128/AAC.49.2.728-732.2005

Rapp, B. E. (2017). Chapter 9 - Fluids. In B. E. B. T.-M. M. Rapp Mechanics and Mathematics (Ed.), *Micro and Nano Technologies* (pp. 243–263). Elsevier. https://doi.org/https://doi.org/10.1016/B978-1-4557-3141-1.50009-5

Raza, W., & Kim, K. Y. (2019). Asymmetrical split-and-recombine micromixer with baffles. *Micromachines*, *10*(12). https://doi.org/10.3390/mi10120844

Rocha, G. N., Poole, R. J., & Oliveira, P. J. (2007). Bifurcation phenomena in viscoelastic flows through a symmetric 1:4 expansion. *Journal of Non-Newtonian Fluid Mechanics*, *141*(1), 1–17. https://doi.org/10.1016/j.jnnfm.2006.08.008

Santana, H. S. S., Silva Jr, J. L., Taranto, O. P. P., Silva, J. L., & Taranto, O. P. P. (2019). Optimization of micromixer with triangular baffles for chemical process in millidevices. *Sensors and Actuators, B: Chemical*, *281*(September 2018), 191–203. https://doi.org/10.1016/j.snb.2018.10.089

Sato, H., Ito, S., Tajima, K., Orimoto, N., & Shoji, S. (2005). PDMS microchannels with slanted grooves embedded in three walls to realize efficient spiral flow. *Sensors and Actuators, A: Physical*, *119*(2), 365–371. https://doi.org/10.1016/j.sna.2004.08.033

Schönfeld, F., & Hardt, S. (2004). Simulation of Helical Flows in Microchannels. *AIChE Journal*, *50*(4), 771–778. https://doi.org/10.1002/aic.10071

Shamloo, A., Vatankhah, P., & Akbari, A. (2017). Analyzing mixing quality in a curved centrifugal micromixer through numerical simulation. *Chemical Engineering and Processing - Process Intensification*, *116*, 9–16. https://doi.org/10.1016/j.cep.2017.03.008

Shi, X., Huang, S., Wang, L., & Li, F. (2019). Numerical analysis of passive micromixer with novel obstacle design. *Journal of Dispersion Science and Technology*, *0*(0), 1–17. https://doi.org/10.1080/01932691.2019.1699428

Shi, X., Wang, L., Huang, S., & Li, F. (2019). A novel passive micromixer with array of Koch fractal obstacles in microchannel. *Journal of Dispersion Science and Technology*, *0*(0), 1–12. https://doi.org/10.1080/01932691.2019.1674156

Ståhl, M., Åslund, B. L., & Rasmuson, Å. C. (2001). Reaction crystallization kinetics of benzoic acid. *AIChE Journal*, *47*(7), 1544–1560. https://doi.org/10.1002/aic.690470708

Sudarsan, A. P., & Ugaz, V. M. (2006). Fluid mixing in planar spiral microchannels. *Lab on a Chip*, *6*(1), 74–82. https://doi.org/10.1039/b511524h

Sun, J., Li, M., Liu, C., Zhang, Y., Liu, D., Liu, W., Hu, G., & Jiang, X. (2012). Double spiral microchannel for label-free tumor cell separation and enrichment. *Lab on a Chip*, *12*(20), 3952–3960. https://doi.org/10.1039/c2lc40679a

The, H. Le, Ta, B. Q., Thanh, H. Le, Dong, T., Thoi, T. N., & Karlsen, F. (2015). Geometric effects on mixing performance in a novel passive micromixer with trapezoidal-zigzag channels. *Journal of Micromechanics and Microengineering*, *25*(9). https://doi.org/10.1088/0960-1317/25/9/094004

Tran-Minh, N., Dong, T., & Karlsen, F. (2014). An efficient passive planar micromixer with ellipse-like micropillars for continuous mixing of human blood. *Computer Methods and Programs in Biomedicine*, *117*(1), 20–29. https://doi.org/10.1016/j.cmpb.2014.05.007

Usefian, A., Bayareh, M., Shateri, A., & Taheri, N. (2019). Numerical study of electro-osmotic micro-mixing of Newtonian and non-Newtonian fluids. *Journal of the Brazilian Society of Mechanical Sciences and Engineering*, *41*(5), 1–10. https://doi.org/10.1007/s40430-019-1739-2

Wang, H., Iovenitti, P., Harvey, E., & Masood, S. (2002). Optimizing layout of obstacles for enhanced mixing in microchannels. *Smart Materials and Structures*, *11*(5), 662–667. https://doi.org/10.1088/0964-1726/11/5/306

Wong, S. H., Bryant, P., Ward, M., & Wharton, C. (2003). Investigation of mixing in a cross-shaped micromixer with static mixing elements for reaction kinetics studies. *Sensors and Actuators, B: Chemical*, *95*(1–3), 414–424. https://doi.org/10.1016/S0925-4005(03)00447-7

Wong, S. H., Ward, M. C. L., & Wharton, C. W. (2004). Micro T-mixer as a rapid mixing micromixer. *Sensors and Actuators, B: Chemical*, *100*(3), 359–379. https://doi.org/10.1016/j.snb.2004.02.008

Xie, T., & Xu, C. (2017). Numerical and experimental investigations of chaotic mixing behavior in an oscillating feedback micromixer. *Chemical Engineering Science*, *171*, 303–317.

Zhang, M., Zhang, W., Wu, Z., Shen, Y., Chen, Y., Lan, C., Li, F., & Cai, W. (2019). Comparison of Micro-Mixing in Time Pulsed Newtonian Fluid and Viscoelastic Fluid. *Micromachines*, *10*(4), 262. https://doi.org/10.3390/mi10040262